

Efficient time-domain scattering synthesis via frequency-domain singularity subtraction

Oscar P. Bruno*

Manuel A. Santana*

Abstract

Fourier-transform-based methods enable accurate, dispersion-free simulations of time-domain scattering problems by evaluating solutions to the Helmholtz equation at a discrete set of frequencies, sufficient to approximate the inverse Fourier transform. However, in the case of scattering by trapping obstacles, the Helmholtz solution exhibits nearly-real complex resonances—which significantly slows the convergence of numerical inverse transform. To address this difficulty this paper introduces a frequency-domain singularity subtraction technique that regularizes the integrand of the inverse transform and efficiently computes the singularity contribution via a combination of a straightforward and inexpensive numerical technique together with a large-time asymptotic expansion. Crucially, all *relevant complex resonances* and their residues are determined via rational approximation of integral equation solutions at *real frequencies*. An adaptive algorithm is employed to ensure that all relevant complex resonances are properly identified.

1 Introduction

Recently developed “Frequency-time-hybrid” (FTH) Fourier-transform-based methods [5, 6] offer accurate and efficient numerical techniques for solving exterior time-domain wave scattering problems; corresponding interior problems can be tackled by such approaches as well [16]. These algorithms solve the associated Helmholtz problems at a discrete set of frequencies—typically using layer potential formulations—combined with specialized techniques such as “windowing-and-recentering” and high-frequency integration, enabling effective reconstruction of the time-domain solution via inverse Fourier transformation. This approach offers several advantages: it produces dispersion-free solutions, enables straightforward parallelization in both space and time, and can efficiently accommodate incident fields that persist indefinitely. However, the performance of these methods is severely impacted by the presence of trapping geometries. In such cases, the Helmholtz solution exhibits nearly real complex resonances (poles), which cause extremely slow convergence in the numerical evaluation of the inverse Fourier transform. This work addresses that challenge through a frequency-domain singularity subtraction technique that regularizes the integrand and naturally transitions to a large-time asymptotic expansion expressed in terms of the complex resonances. These resonances and their residues are evaluated efficiently using only real-frequency data, via a novel Incidence Excited (IE) adaptive algorithm that employs rational approximation in the frequency variable. The resulting overall FTH-SS (Singularity-Subtraction FTH) approach enables accurate and efficient time-domain scattering simulations, for arbitrarily long time, even for highly-trapping scattering structures.

Other methods, notably the well known Convolution Quadrature (CQ) method [8, 11, 36] have been presented that, like the FTH methods, rely on transformation into the frequency domain. A detailed discussion of certain advantages offered by the FTH algorithms in relation to other frequency-time approaches (relating, in the case of the CQ method, to time dispersion and existence of an infinite tail), can be found

*Computing and Mathematical Sciences, California Institute of Technology, Pasadena, CA, 91125 USA, obruno@caltech.edu, msantana@caltech.edu)

in [5] and will therefore not otherwise be discussed here. We note, however, that the use of the singularity subtraction and IE resonance evaluation algorithms introduced in this paper might have a beneficial impact in the context of the CQ methodology as well.

The difficulties faced by the FTH method in trapping configurations can be traced to the frequency-dependent behavior of the scattering solutions. Indeed, for obstacles which are strongly trapping (see e.g. [4, 31] for more precise definitions of the concept of trapping scatterer), the frequency domain scattering solutions typically exhibit nearly real poles as functions of frequency. These complex resonances manifest as sharp, spike-like features along the real frequency axis [10, 19, 31, 48], which require a dense sampling of frequency points to resolve, thereby making the numerical inversion of the Fourier transform prohibitively expensive.

An additional difficulty in evaluating time domain scattering by trapping obstacles relates to the slow temporal decay of the scattered field in trapping regions. This phenomenon has been the focus of extensive analytical work, which connects the decay rate to the geometric properties of the scatterer [4, 29, 32, 33, 44, 45, 52]. The slow decay associated with trapping poses challenges for traditional time-domain methods such as finite difference and finite element based techniques, which require fine spatial and temporal resolution to control dispersion errors over long simulation times. For long time evaluation of the scattered field a popular alternative is to express the scattered field as an asymptotic “singularity expansion” [9] in terms of the complex resonances. Such expansions can be formally derived on the basis of evaluation of the inverse Fourier-transform via contour deformation, where for late enough times the contribution from the poles dominate. Much work has gone into proving the validity of the aforementioned singularity expansions [33, 52, 54], although a rigorous justification for their validity in the trapping case remains elusive. Nevertheless, singularity expansions have been widely used in practice to model late-time scattering phenomena [9, 27, 28, 38, 41, 42, 57], although not without criticism of the formalism sometimes used [20, 28, 49]. The numerical examples presented in this paper—including problems involving scattering by highly-trapping obstacles—provide strong evidence for the validity and high accuracy of the singularity expansion in the asymptotic regime, regardless of the trapping character of the scatterer.

This contribution proposes a method for evaluation of the slowly decaying scattered fields from trapping obstacles which relies on a certain frequency-domain singularity subtraction methodology. Subtraction of complex resonances and their residues near the real axis regularizes the integrand of the inverse Fourier-transform leading to greatly increased convergence of numerical quadrature rules. The contributions from the complex resonances are computed using a numerical algorithm that partially relies on the singularity expansion mentioned above (Section 4.2). Importantly the proposed method is valid, independently of the validity of the aforementioned singularity expansion, asymptotic or otherwise.

A key element contributing to the efficiency of the proposed method is the aforementioned Incident-Excited (IE) algorithm, which identifies complex resonances excited by a specific incident field using only real-frequency Helmholtz solutions. This stands in contrast to traditional approaches for computing complex resonances [2, 7, 12, 24, 26, 43], which require solving the Helmholtz equation at complex frequencies. The exclusive use of real-frequency data is made possible through AAA rational approximation [15, 47], and indeed the IE method introduced in this paper can be viewed as an extension of the resonance evaluation technique introduced in [15].

This paper is structured as follows. Section 2 introduces the time-domain scattering problem, and provides an overview of the Frequency-time hybrid method. The relevant frequency-domain integral equations and their connection to complex resonances is also discussed in that section. Section 3 presents the AAA algorithm for rational approximation [47] and related variants, leading to the introduction of the novel Incident-Excited algorithm for efficiently computing the resonances excited by a given incident field. In Section 4, the singularity subtraction procedure is described in detail, along with a numerical technique for evaluating the singular contributions and their asymptotic expansion. Section 5 then provides a complete description of the FTH-SS method. Finally, Section 6 presents numerical experiments that demonstrate the accuracy and effectiveness of the proposed approach. These results highlight the features of the incidence-

excited resonance evaluation algorithm, the smoothing effects of the singularity subtraction strategy, the accuracy and convergence of the overall methodology, its capacity for efficient long-time simulation, and compelling numerical evidence supporting the validity of the singularity expansion in highly trapping configurations.

2 Preliminaries

We are concerned with the problem of scattering of waves governed by the wave equation

$$\frac{\partial^2 u}{\partial t^2}(\mathbf{r}, t) - c^2 \Delta u(\mathbf{r}, t) = 0, \quad \mathbf{r} \in \Omega^e \quad (1a)$$

$$u(\mathbf{r}, 0) = \frac{\partial u}{\partial t}(\mathbf{r}, 0) = 0, \quad \mathbf{r} \in \Omega^e \quad (1b)$$

$$u(\mathbf{r}, t) = b(\mathbf{r}, t) \quad \text{for} \quad (\mathbf{r}, t) \in \Gamma \times [0, T^{\text{inc}}] \quad (1c)$$

where $\Omega^e \subset \mathbb{R}^2$ is an “exterior domain” with boundary Γ , which equals either the exterior of a *closed* curve Γ (such as e.g. the unit circle) or the complement of an *open* curve Γ (such as a straight segment, a circular section, etc.). The methods and ideas to be developed, which concern the frequency-time duality, should be applicable in both 2D and 3D contexts, but, for the sake of simplicity, this paper is restricted to the 2D context only. For a given incident field u^{inc} defined in the exterior of Γ , the solution u of the problem (1) with boundary values $b = -u^{\text{inc}}$ is the “scattered field”; the total field in the exterior of Γ is thus given by $u^{\text{tot}}(\mathbf{r}, t) = u^{\text{inc}}(\mathbf{r}, t) + u(\mathbf{r}, t)$. With these notations, the time domain boundary conditions (1c) become

$$u^{\text{tot}}(\mathbf{r}, t) = u^{\text{inc}}(\mathbf{r}, t) + u(\mathbf{r}, t) = 0, \quad \mathbf{r} \in \Gamma. \quad (2)$$

To solve equation (1) we build upon the Fourier transform based method recently introduced in [5], which we refer to henceforth as the frequency-time hybrid method (FTH). In brief, the FTH method utilizes the Fourier transforms $U = U(\mathbf{r}, \omega)$ and $B = B(\mathbf{r}, \omega)$ of the functions u and b with respect to time, respectively. It obtains U as the solution of the Helmholtz equation problem

$$\Delta U(\mathbf{r}, \omega) + \kappa^2(\omega) U(\mathbf{r}, \omega) = 0, \quad \mathbf{r} \in \Omega^e \quad (3a)$$

$$U(\mathbf{r}, \omega) = B(\mathbf{r}, \omega) \quad \mathbf{r} \in \Gamma, \quad (3b)$$

$$\lim_{|\mathbf{r}| \rightarrow \infty} \sqrt{|\mathbf{r}|} \left(\frac{\partial U}{\partial |\mathbf{r}|} - i\kappa(\omega) U \right) = 0, \quad \text{uniformly in all directions } \mathbf{r}/|\mathbf{r}| \quad (3c)$$

with linear dispersion relation $\kappa = \kappa(\omega) = \omega/c$, and where i denotes the complex unit. It then produces the time-domain solution $u(\mathbf{r}, t)$ as the inverse Fourier transform of U .

As pointed out in [5], a straightforward application of these ideas presents a number of difficulties which, however, may be effectively bypassed to yield an effective, fast and accurate time-domain computational technique for the solution of the problem (1). A brief discussion concerning these challenges and their resolution is presented in Section 2.1. Then the method of boundary integral operators for computing the solution to the Helmholtz problem (3) for open and closed curves are reviewed in Section 2.2. Certain specialized high-frequency quadrature rules that are used in the inverse Fourier transform process are outlined in Section 2.3, and finally a brief discussion of complex resonances is given in Section 2.4.

2.1 Frequency-time hybrid method

For definiteness throughout this paper we restrict attention to one of the most commonly occurring boundary conditions, namely, incident fields which impinge along a single direction \mathbf{p} —so that $b(\mathbf{r}, t) = a(t - \mathbf{p} \cdot \mathbf{r}/c)$ —but general boundary conditions can be treated similarly [6]. Further, the function $a(t)$ is assumed infinitely

smooth and compactly supported in the interval $[0, T^{\text{inc}}]$; see also Remark 1. Under this assumption the boundary condition function $b(\mathbf{r}, t)$ in (1c) may be expressed in the form

$$b(\mathbf{r}, t) = \frac{1}{2\pi} \int_{-\infty}^{\infty} A(\omega) B_{\mathbf{p}}(\mathbf{r}, \omega) e^{-i\kappa(\omega)ct} d\omega, \quad \text{where} \quad A(\omega) = \int_{-\infty}^{\infty} a(t) e^{i\omega t} dt, \quad (4)$$

and where

$$B_{\mathbf{p}}(\mathbf{r}, \omega) = e^{i\kappa(\omega)\mathbf{p}\cdot\mathbf{r}} \quad (5)$$

—with integrals that can be produced with high accuracy by means of the FTH specialized quadrature rules reviewed in this section and Section 2.3.

Remark 1. The proposed Fourier transform approach can continued to be used with high accuracy even when the time-domain boundary data $b(t)$ or the function $a(t)$ do not vanish at $t = T^{\text{inc}}$. This is achieved by suitably extending the given function to one that vanishes smoothly for some time $T > T^{\text{inc}}$; by causality, the resulting solution u coincides with the solution sought up to time $t = T^{\text{inc}}$.

The direct computation of $A(\omega)$ according to equation (4) presents certain challenges for large values of T^{inc} —that is to say, in cases for which the incidence-field function $a(t)$ continues to take non-vanishing values up to large times t . Indeed, for such large t values the exponential factor $e^{i\omega t}$ in the second integral of (4) is highly oscillatory with respect to ω . Consequently, the integral $A(\omega)$ also becomes highly oscillatory, and, thus, its evaluation over a dense set of frequency points is necessary to ensure adequate sampling. This, in turn, requires the solution of frequency-domain problems for a large number of frequencies ω , resulting in significant computational costs.

To tackle this and related issues concerning high-frequency integration, a partition-of-unity set $\{w_k(t) : k = 1, \dots, K\}$ of windowing functions is used, where each function w_k is supported in the interval $[s_k - H, s_k + H]$ for a corresponding support center $s_k \in [0, T^{\text{inc}}]$ and k -independent window size H , and where the functions w_k satisfy the “partition-of-unity” property

$$\sum_{k=1}^K w_k(t) = 1 \quad \text{for} \quad t \in [0, T^{\text{inc}}]. \quad (6)$$

In this work we use the window functions $w_k(t) = w(t - s_k)$ where

$$w(t; H) = w(t) = \begin{cases} 1, & |t| < \alpha \\ \frac{1}{2} \operatorname{erfc} \left[-\rho + 2\rho \left(\frac{|t| - \alpha H}{(1 - \alpha)H} \right) \right], & \alpha H \leq |t| \leq H \\ 0, & |t| > H. \end{cases} \quad (7)$$

For a given window size H the partition of unity condition (6) can be made to hold by appropriately choosing the centers s_k —as it follows easily from the fact that $\operatorname{erf}(t) = 1 - \operatorname{erfc}(t)$ is an odd function of z . Note that, while the functions $w_k(t)$ obtained in this fashion are not strictly compactly supported, they do tend to zero exponentially fast as t grows, and they essentially vanish at $t - s_k = H$, to any prescribed numerical precision ε^{np} , provided the value of the parameter ρ is selected appropriately. Throughout this paper the values, $\alpha = 0.5$, and $\rho = 5.805$ was used, for which $|w(t)| \leq \varepsilon^{\text{np}} = 1.1 \cdot 10^{-16}$ for $|t| \geq H$, with a corresponding departure from one of less than ε^{np} for $|t| = \alpha H$. Following [5, sec. 3.1] in all cases we set $s_k = 3(k - 1)H/2$ and $H = 10$.

Letting $a_k(t) = w_k(t)a(t)$ we write

$$A(\omega) = \sum_{k=1}^K A_k(\omega) \quad \text{where} \quad A_k(\omega) = \int_{s_k - H}^{s_k + H} a_k(t) e^{i\omega t} dt. \quad (8)$$

A change of variables to recenter the integration around the origin gives

$$A_k(\omega) = \int_{-H}^H a_k(t) e^{i\omega(t+s_k)} dt = e^{i\omega s_k} \int_{-H}^H a_k(t) e^{i\omega t} dt = e^{i\omega s_k} A_k^{\text{slow}}(\omega) \quad (9)$$

where $A_k^{\text{slow}}(\omega)$ is defined, as implied by the notation in equation (9), to equal the second integral in that equation.

Remark 2. Clearly, A_k^{slow} is a “slowly varying” function of ω , in that its derivatives with respect to ω are uniformly bounded for all k , provided a , and, thus, a_k for all k , are bounded functions of t . As a result these functions may be represented numerically on the basis of their values at fixed numbers of discretization points.

For $k = 1, \dots, K$ we then define windowed time domain boundary functions

$$b_k(\mathbf{r}, t) = \frac{1}{2\pi} \int_{-\infty}^{\infty} A_k(\omega) B_{\mathbf{p}}(\mathbf{r}, \omega) e^{-i\kappa(\omega)ct} d\omega = \frac{e^{i\omega s_k}}{2\pi} \int_{-\infty}^{\infty} A_k^{\text{slow}}(\omega) B_{\mathbf{p}}(\mathbf{r}, \omega) e^{-i\kappa(\omega)ct} d\omega. \quad (10)$$

Then denoting by $u_k(\mathbf{r}, t)$ the solution to (1) with $b(\mathbf{r}, t)$ replaced with $b_k(\mathbf{r}, t)$ we obtain

$$u(\mathbf{r}, t) = \sum_{k=1}^K u_k(\mathbf{r}, t). \quad (11)$$

It is important to note that, since $a(t)$ and $a_k(t)$ are infinitely smooth and compactly supported functions they are also essentially band limited: the related Fourier transforms $A(\omega)$, $A_k(\omega)$ and $A_k^{\text{slow}}(\omega)$ tend to zero faster than any power of ω as $|\omega| \rightarrow \infty$. Thus, for a certain interval

$$I = [W_1, W_2] \quad (12)$$

we have (cf. (78))

$$A(\omega) \approx 0, \quad A_k(\omega) \approx 0, \quad \text{and} \quad A_k^{\text{slow}}(\omega) \approx 0 \quad \text{for} \quad \omega \notin I. \quad (13)$$

Letting $U_k(\mathbf{r}, \omega)$ and $U_k^{\text{slow}}(\mathbf{r}, \omega)$ denote the solutions of equation (3) with boundary values $B(\mathbf{r}, \omega) = A_k(\omega) B_{\mathbf{p}}(\mathbf{r}, \omega)$ and $B(\mathbf{r}, \omega) = A_k^{\text{slow}}(\omega) B_{\mathbf{p}}(\mathbf{r}, \omega)$, respectively, it follows that $u_k(\mathbf{r}, t)$ may be expressed in the forms

$$u_k(\mathbf{r}, t) = \frac{1}{2\pi} \int_{-\infty}^{\infty} U_k(\mathbf{r}, \omega) e^{-i\omega t} d\omega = \frac{1}{2\pi} \int_{-\infty}^{\infty} U_k^{\text{slow}}(\mathbf{r}, \omega) e^{-i\omega(t-s_k)} d\omega.$$

Further, in view of (13) it follows that

$$U(\omega) \approx 0, \quad U_k(\omega) \approx 0, \quad \text{and} \quad U_k^{\text{slow}}(\omega) \approx 0 \quad \text{for} \quad \omega \notin I. \quad (14)$$

Thus $u_k(\mathbf{r}, t)$ is closely approximated by a strictly band limited function $u_k^I(\mathbf{r}, t)$,

$$u_k(\mathbf{r}, t) \approx u_k^I(\mathbf{r}, t) = \frac{1}{2\pi} \int_{W_1}^{W_2} U_k^{\text{slow}}(\mathbf{r}, \omega) e^{-i\omega(t-s_k)} d\omega, \quad (15)$$

with errors that decay super-algebraically fast as the bandwidth grows, uniformly for $(\mathbf{r}, t) \in \Omega^e \times \mathbb{R}$ and $k \in \mathbb{N}$. The wave equation solution (11) may then be approximated by a band limited counterpart

$$u(\mathbf{r}, t) \approx u^I(\mathbf{r}, t) := \sum_{k=1}^K u_k^I(\mathbf{r}, t). \quad (16)$$

The frequency-domain solutions $U_k^{\text{slow}}(\mathbf{r}, \omega)$ may be obtained by means of any available Helmholtz solver. However, due to their efficiency and flexibility we compute $U_k^{\text{slow}}(\mathbf{r}, \omega)$ by means of layer potential methods, which are reviewed in the following section.

2.2 Frequency-domain integral equation solutions

We consider first the case in which Γ is a closed curve. Define the single-layer $\mathcal{S}_\omega[\psi](\mathbf{r})$ and double-layer potentials $\mathcal{K}_\omega[\psi](\mathbf{r})$ for a certain density function ψ ,

$$\mathcal{S}_\omega[\psi](\mathbf{r}) = \int_{\Gamma} G_\omega(\mathbf{r}, \mathbf{r}') \psi(\mathbf{r}', \omega) d\sigma(\mathbf{r}') \quad \text{and} \quad \mathcal{K}_\omega[\psi](\mathbf{r}) = \int_{\Gamma} \frac{\partial G_\omega(\mathbf{r}, \mathbf{r}')}{\partial n(\mathbf{r}')} \psi(\mathbf{r}', \omega) d\sigma(\mathbf{r}'), \quad \mathbf{r} \in \Omega^e \quad (17)$$

where

$$G_\omega(\mathbf{r}, \mathbf{r}') = \frac{i}{4} H_0^1 \left(\frac{\omega}{c} |\mathbf{r} - \mathbf{r}'| \right)$$

denotes the 2D Green function, where H_0^1 is the zeroth-order Hankel function of the first kind. Then for closed curves the solution U of the Helmholtz problem (3) can be represented in the combined-field form

$$U(\mathbf{r}, \omega) = \mathcal{C}_{\omega, \eta}[\psi](\mathbf{r}, \omega) := \mathcal{K}_\omega[\psi](\mathbf{r}, \omega) - i\eta \mathcal{S}_\omega[\psi](\mathbf{r}, \omega), \quad \mathbf{r} \in \Omega^e, \quad (18)$$

where $\eta \in \mathbb{R}$, $\eta \neq 0$. Using the frequency domain single- and double-layer operators

$$(S_\omega \psi)(\mathbf{r}) = \int_{\Gamma} G_\omega(\mathbf{r}, \mathbf{r}') \psi(\mathbf{r}', \omega) d\sigma(\mathbf{r}') \quad \text{and} \quad (K_\omega \psi)(\mathbf{r}) = \int_{\Gamma} \frac{\partial G_\omega(\mathbf{r}, \mathbf{r}')}{\partial n(\mathbf{r}')} \psi(\mathbf{r}', \omega) d\sigma(\mathbf{r}'), \quad \mathbf{r} \in \Gamma, \quad (19)$$

respectively, and defining the combined-field boundary integral operator

$$(C_{\omega, \eta} \psi) := \frac{1}{2} \psi(\mathbf{r}, \omega) + (K_\omega \psi)(\mathbf{r}) - i\eta (S_\omega \psi)(\mathbf{r}), \quad \mathbf{r} \in \Gamma. \quad (20)$$

the density $\psi(\mathbf{r}', \omega)$ may be obtained as the unique solution of the integral equation

$$(C_{\omega, \eta} \psi) = B(\mathbf{r}, \omega), \quad \mathbf{r} \in \Gamma. \quad (21)$$

As is well known the representation (21) is not applicable in case Γ is an open curve. In such cases, the solution of the Helmholtz problem (3) may instead be represented in the form

$$U(\mathbf{r}, \omega) = \mathcal{S}_\omega[\phi](\mathbf{r}, \omega), \quad \mathbf{r} \in \Omega^e \quad (22)$$

where ϕ denotes the unique solution of the boundary integral equation

$$(S_\omega \phi)(\mathbf{r}) = B(\mathbf{r}, \omega), \quad \mathbf{r} \in \Gamma. \quad (23)$$

The numerical implementations used in this paper for the closed-curve operator (20) are based on the Nyström methods [18, sec. 3.6]. The corresponding implementations [13] for the single-layer operator, in turn, are used for the open-arc problem. Following the latter reference, in particular, in the open arc case a smooth parametrization $\mathbf{r} = \mathbf{r}(t)$ of Γ ($-1 \leq t \leq 1$) is used to express the integral density ϕ in the form

$$\phi(\mathbf{r}(t')) = \psi(\mathbf{r}(t')) / \sqrt{1 - t'^2}, \quad (24)$$

where ψ is a smooth function, and where the square-root denominator explicitly accounts for the singularities of the density ϕ at the edges of the open curve Γ . Clearly we may write

$$(S_\omega^{\text{arc}} \psi) = (S_\omega \phi), \quad (25)$$

for a certain operator S_ω^{arc} [13, 35], and equation (23) becomes

$$(S_\omega^{\text{arc}} \psi)(\mathbf{r}) = B(\mathbf{r}, \omega), \quad \mathbf{r} \in \Gamma; \quad (26)$$

the solution U , given by equation (22) with ϕ re-expressed in terms of ψ via equation (24), can be written as

$$U(\mathbf{r}, \omega) = \mathcal{S}_\omega^{\text{arc}}[\psi](\mathbf{r}, \omega), \quad \mathbf{r} \in \Omega^e \quad (27)$$

for a certain operator $\mathcal{S}_\omega^{\text{arc}}$. (An application of the change of variables $t' = \cos(\theta')$ in the $\mathbf{r} = \mathbf{r}(t')$ parametrized version of equation (26) produces a Jacobian which exactly cancels the (explicit) edge singularity, and, further, it enables the representation of the singular function ϕ in terms of a rapidly convergent cosine series for the smooth density ψ . The open-curve algorithm is completed [13] by exploiting a quadrature rule that leverages exact integration of the product of cosine Fourier basis functions and a logarithmic kernel.)

Throughout this paper the symbol H_ω is used to denote either $C_{\omega, \eta}$ or S_ω^{arc} , depending on context:

$$H_\omega = C_{\omega, \eta} \quad \text{for closed curve problems, and} \quad H_\omega = S_\omega^{\text{arc}} \quad \text{for open arc problems.} \quad (28)$$

Clearly, the function U_k^{slow} in (15), that is required by the FTH method to produce the k -th time-domain solution u_k , is the solution of the Helmholtz equation (3) with boundary values related to $B_{\mathbf{p}}(\mathbf{r}, \omega)$ in (5):

$$B(\mathbf{r}, \omega) = A_k^{\text{slow}}(\omega) B_{\mathbf{p}}(\mathbf{r}, \omega) = A_k^{\text{slow}}(\omega) e^{i\kappa(\omega)\mathbf{p} \cdot \mathbf{r}}. \quad (29)$$

As indicated in what follows, the functions U_k^{slow} may be efficiently obtained, for both closed- and open-curve problems, on the basis of the integral formulations just described. To achieve this, we define

$$\mathcal{F} = \{\omega_1, \dots, \omega_J\} \subset I \quad (30)$$

(see (12)) a k -independent set of J equispaced frequencies, which is assumed to be sufficient for evaluating the integral in (15)—for all k and within a given error tolerance—once again by means of the FTH specialized quadrature rules based on windowing and recentering described in Section 2.3. Further, letting

$$\psi_{\mathbf{p}}(\mathbf{r}', \omega) = \text{“Solution } \psi = \psi(\mathbf{r}', \omega) \text{ of (21) or (26), as applicable, with } B(\mathbf{r}, \omega) = B_{\mathbf{p}}(\mathbf{r}, \omega)\text{”}. \quad (31)$$

we define the k -independent density-solution set

$$\mathcal{D}_{\mathcal{F}} = \{\psi_{\mathbf{p}}(\mathbf{r}', \omega_j) : 1 \leq j \leq J\}. \quad (32)$$

Calling

$$U_{\mathbf{p}}(\mathbf{r}, \omega) \text{ the Helmholtz solution given by (18) or (27), as applicable, with density } \psi = \psi_{\mathbf{p}}, \quad (33)$$

(wherein, clearly, $U_{\mathbf{p}}$ is independent of k , and where $\psi_{\mathbf{p}}$ is expressed in terms of a corresponding density $\phi_{\mathbf{p}}$, in accordance with (24), in the open-arc case), the k -th Helmholtz solution $U_k^{\text{slow}}(\mathbf{r}, \omega_j)$ ($1 \leq j \leq J$), which takes on the boundary values (29) for $\mathbf{r} \in \Gamma$, is given by

$$U_k^{\text{slow}}(\mathbf{r}, \omega_j) = A_k^{\text{slow}}(\omega_j) U_{\mathbf{p}}(\mathbf{r}, \omega_j). \quad (34)$$

Thus, as suggested above, the k -independent set of solutions $\mathcal{D}_{\mathcal{F}}$ suffices to evaluate the necessary functions U_k^{slow} for all k .

In what follows the discrete forms (given in [18, sec. 3.6] and [35], respectively) of the operators $C_{\omega, \eta}$ and S_ω^{arc} in (20) and (25) on an N -point discretization $\{\mathbf{r}_1, \dots, \mathbf{r}_N\}$ of Γ are respectively denoted by

$$C_{\omega, \eta}^N \quad \text{and} \quad S_\omega^{\text{arc}, N}. \quad (35)$$

Paralleling (28) we let

$$\tilde{H}_\omega = C_{\omega, \eta}^N \quad \text{for closed curve problems, and} \quad \tilde{H}_\omega = S_\omega^{\text{arc}, N} \quad \text{for open arc problems.} \quad (36)$$

The corresponding numerical solutions of (21) or (26), as applicable, with discrete boundary values

$$\tilde{B}_{\mathbf{p}}(\omega) = (\tilde{B}_{\mathbf{p}, 1}(\omega), \dots, \tilde{B}_{\mathbf{p}, N}(\omega)) = (e^{i\kappa(\omega)\mathbf{p} \cdot \mathbf{r}_i})_{i=1}^N \quad (37)$$

(cf. (5)), are denoted by

$$\tilde{\psi}_{\mathbf{p}}(\omega) = \tilde{H}_\omega^{-1} \tilde{B}_{\mathbf{p}}(\cdot, \omega); \quad \tilde{\psi}_{\mathbf{p}}(\omega) = (\tilde{\psi}_{\mathbf{p}, 1}, \dots, \tilde{\psi}_{\mathbf{p}, N}) \approx (\psi_{\mathbf{p}}(\mathbf{r}_1, \omega), \dots, \psi_{\mathbf{p}}(\mathbf{r}_N, \omega)). \quad (38)$$

2.3 $O(1)$ -cost Fourier transform at large times

While, as indicated in Remark 2, A_k^{slow} is a slowly oscillatory function of ω , the numerical evaluation of the integral in (15) still requires the use of increasingly finer discretization meshes as t grows, on account of the fast oscillations exhibited by the exponential term $e^{-i\omega(t-s_k)}$, as function of ω for large t . As a result, the evaluation of the quantity $u_k^I(\mathbf{r}, t)$ by means of classical quadrature rules requires increasingly fine frequency meshes, and, thus, increasing numbers of expensive Helmholtz-equation solutions, as t increases. The FTH algorithm [5] addresses this challenge by employing $O(1)$ -cost high-frequency integration methods, which are reviewed in Sections 2.3.1 and 2.3.2, for general integrals of the form

$$\mathcal{I}^{[a,b]}[F](t) = \int_a^b F(\omega) e^{-i\omega t} d\omega. \quad (39)$$

In view of the logarithmic singularities exhibited by the solutions of the 2D Helmholtz equation as functions of ω at $\omega = 0$ [37, 56], in what follows we assume that $F(\omega)$ has a logarithmic singularity at $\omega = 0$ but is otherwise smooth, and we separately discuss the quadrature problem for the cases $0 \notin [a, b]$ and $0 \in [a, b]$.

2.3.1 Vanishing zero frequency-content case

In order to evaluate the integral (39) in the case in which $F(\omega)$ is smooth for $\omega \in [a, b]$ we first re-express that integral in the form

$$\mathcal{I}^{[a,b]}[F](t) = e^{-i\delta t} \int_{-W}^W F(\delta + \omega) e^{-i\omega t} d\omega \quad \text{where} \quad W = \frac{b-a}{2} \quad \text{and} \quad \delta = \frac{b+a}{2}. \quad (40)$$

The function $F(\delta + \omega)$ is then approximated by a trigonometric polynomial of the form

$$F(\delta + \omega) \approx \sum_{m=-M/2}^{M/2-1} c_m e^{i\frac{2\pi}{P}m\omega}, \quad (41)$$

where M and P are to be selected appropriately. In the case that $F(\delta + \omega)$ can be extended as a periodic and smooth function of period $2A$ the value $P = 2A$ is selected, and the trigonometric polynomial (41) is obtained by standard techniques, and with an approximation error that decays faster than any negative power of M as M grows. If $F(\delta + \omega)$ is not $2A$ -periodic, on the other hand, an accurate Fourier approximation with period $P > 2A$ is obtained by means of the FC(Gram) Fourier continuation method [3, 14], with errors that decay as a user-prescribed negative power of M .

To complete the quadrature rule we write $\alpha = \frac{P}{2\pi}$, substitute (41) into (40) and integrate termwise—which results in the highly accurate approximation

$$\mathcal{I}^{[a,b]}[F](t) \approx e^{-i\delta t} \sum_{m=-M/2}^{M/2-1} c_m \frac{P}{\pi(\alpha t - m)} \sin\left(\pi \frac{2W}{P}(\alpha t - m)\right) \quad (42)$$

which may be obtained at fixed cost for arbitrarily large values of t . As noted in [5], finally, the expression (42) may be produced over prescribed equispaced sets of times t at FFT speeds by employing the fractional Fourier transform.

2.3.2 Non-vanishing zero frequency content case

In the case in which $0 \in [a, b]$ and $F(\omega)$ has a logarithmic singularity at $\omega = 0$ we first re-express the integral (39) in the form

$$\mathcal{I}^{[a,b]}[F](t) = \left(\int_a^{-w_c} + \int_{-w_c}^{w_c} + \int_{w_c}^b \right) F(\omega) e^{-i\omega t} d\omega. \quad (43)$$

The first and third integrals may be treated by the quadrature rule described in section 2.3.1. The integral in the interval $[-w_c, w_c]$, in turn, is first reduced to a sum of two integrals of the form

$$\mathcal{I}^{[0, w_c]}[F](t) = \int_0^{w_c} F(\omega) e^{-i\omega t} d\omega,$$

each one of which is evaluated by means of the modified ‘‘Filon-Clenshaw-Curtis’’ quadrature approach [21].

In summary, the classical Filon-Clenshaw-Curtis quadrature rule [50], which assumes $F(\omega)$ is smooth, enables accurate computation of Fourier transforms by approximating F with its truncated Chebyshev series and employing a stable procedure for evaluating integrals where the integrand is a Chebyshev polynomial multiplied by a complex exponential. The modified Filon-Clenshaw-Curtis rule, in turn, introduces a certain graded mesh to resolve the logarithmic singularity, which is subsequently used to form subintervals where the classical Filon-Clenshaw-Curtis rule is applied. Letting M_I and q denote the number of subintervals and the number of integration nodes per subinterval, respectively, the analysis [21] shows that, for fixed M_I , the error in the modified Filon-Clenshaw-Curtis rule decays like $M_I^{-(1+q)}$ as $q \rightarrow \infty$ uniformly for all $t \in \mathbb{R}$.

2.4 Complex resonances

Let $\mathcal{U} = \mathcal{U}_\omega$ denote the solution operator to the Helmholtz problem for either open or closed curves at a given frequency ω : for a given ‘‘boundary-values’’ function $B = B(\mathbf{r})$ in the space H equal to $H^{1/2}(\Gamma)$ for closed curves and equal to $\tilde{H}^{-1/2}(\Gamma)$ for open curves, we have

$$\mathcal{U}[B] = U, \quad \text{where } U \text{ solves the problem (3).} \quad (44)$$

(For detailed definitions of the spaces $H^{1/2}(\Gamma)$ and $\tilde{H}^{-1/2}(\Gamma)$ respectively see [40] and [35]). Using the notation $B = B_\omega$ to explicitly denote the ω -dependence of the given boundary data that is often found in practice, we also write e.g.

$$\mathcal{U} = \mathcal{U}_\omega \quad \mathcal{U} = \mathcal{U}_\omega[B] = \mathcal{U}_\omega[B_\omega] \quad \text{and} \quad U(\mathbf{r}, \omega) = \mathcal{U}_\omega[B_\omega](\mathbf{r}). \quad (45)$$

for the solution operator, the solution U and the values of the solution U for given ω and \mathbf{r} , as needed. As is well known [53] the operator \mathcal{U}_ω , which is defined for all real values of ω , admits a meromorphic continuation into the complex ω plane, with all poles of \mathcal{U}_ω contained in the lower half plane; in the 2D case a branch cut must also be introduced in order to account for a logarithmic singularity at $\omega = 0$. Henceforth, we refer to the poles of \mathcal{U}_ω as complex resonances. The analytic continuation is performed by expressing \mathcal{U}_ω in terms of integral operators. In detail, denoting by $\mathcal{U}_o[\omega]$ for the solution operator for open curves we may write

$$\mathcal{U}_\omega^o[B] = \mathcal{S}_\omega[(S_\omega)^{-1}B].$$

Letting $\mathcal{U}_c[\omega]$ denote the operator for closed curves, except for certain real frequencies ω_j we may write

$$\mathcal{U}_\omega^c[B] = \mathcal{K}_\omega[(K_\omega)^{-1}B], \quad (46)$$

and near real frequencies ω_j which where K_ω is not invertible we write

$$\mathcal{U}_\omega^c[B] = \mathcal{K}_\omega[(C_{\omega, \eta})^{-1}B](\omega) - i\eta \mathcal{S}_\omega[(C_{\omega, \eta})^{-1}B]. \quad (47)$$

See [53] for the full details. Thus, the ω -dependent boundary integral operators, utilized to derive the analytic continuation of $\mathcal{U}(\omega)$, also enable the numerical computation of complex resonances—which correspond to the poles of the resolvents of these operators. This approach is applicable to both closed curves [51] and open arcs [15, sec. 2]. In detail, for open curves the poles of the inverse Single Layer Potential $(S_\omega)^{-1}$ in the

lower half plane correspond to the complex resonances of the scatterer, and, thus the complex resonances may be approximated numerically as the poles of the discrete operator $(S_\omega^N)^{-1}$ in (35). In the case of closed curves, on the other hand, special care must be taken in choosing the combined field coupling parameter η in (18). Indeed, as established in [51] for a certain combined field operator $\tilde{C}_{\omega,\eta}$ associated with the Neumann problem, choosing a coupling parameter $\eta > 0$ causes the inverse $(\tilde{C}_{\omega,\eta})^{-1}$ to have poles in the lower half-plane that do not correspond to complex resonances. However, for $\eta < 0$, these issues do not arise, and the poles of $(\tilde{C}_{\omega,\eta})^{-1}$ in the lower half-plane exactly match the Neumann complex resonances. Appendix A presents a corresponding discussion concerning the operator $C_{\omega,\eta}$ (eq. (20)) associated with the Dirichlet problem, showing that the poles of $(C_{\omega,\eta})^{-1}$ with $\eta < 0$ exactly match the complex resonances of $\mathcal{U}(\omega)$.

The most physically relevant complex resonances are those close to the real axis, as they produce near-singular behavior in the integrand of the inverse Fourier transform integral (15), making its numerical evaluation challenging. A novel algorithm for obtaining all such relevant “incidence-excited” complex resonances for the Dirichlet problem is introduced in Section 3. Notably, the proposed algorithm for evaluation of incidence-excited resonances relies solely on values of the inverse $(C_{\omega,\eta})^{-1}$ at real values of ω . Then the resolution of these challenges by a certain singularity subtraction technique, as well as a crucial connection to the long-time asymptotic behavior of time-domain scattering solutions, is discussed in Section 4.

Remark 3. For simplicity, this paper focuses on the generic case [1,30], where complex resonances are simple poles of \mathcal{U}_ω .

3 Incidence-excited resonances from real-frequency data

Well-known methods [7,9,12] for the evaluation of complex resonances within a contour $\mathcal{C} \subset \mathbb{C}$ require inversion of boundary integral operators along \mathcal{C} . However, most relevant to this work are the complex resonances which both lie near the real axis and are excited by a given incident field. This section proposes a method that, relying on a *new real-axis adaptive* rational approximation strategy, obtains the relevant excited complex resonances on the basis of inversion of the boundary integral operators *at real frequencies only*. The excited frequencies thus obtained can then be utilized in a seamless manner in conjunction with the FTH method to produce the time-domain solution of a given time domain problem.

The groundwork of the method is laid in Section 3.1, starting with a brief presentation of the AAA algorithm for rational approximation [47] and relevant variants. Section 3.2 then motivates the proposed algorithm by reviewing a recently introduced adaptive algorithm [15] for the evaluation of real and complex resonances. Section 3.3 then details the proposed adaptive algorithm for the evaluation of the excited resonances and the corresponding residues,—which, as is demonstrated Section 4, form a basis for the evaluation of time-domain fields at all times with minimal computational cost.

3.1 Scalar-valued and random-sketching vector-valued rational approximation

The AAA algorithm [47] is an efficient method for constructing rational approximants $r^m(\omega) \approx f(\omega)$ for a complex-variable function f on the basis of the values of f at an M -point set $Z \subset \mathbb{C}$. The algorithm proceeds by inductively constructing, for $m = 1, 2, \dots$, certain sets of “support points” $Z_m = \{\omega_1, \dots, \omega_m\}$, $Z_m \subset Z$ ($\omega_p \neq \omega_q$ for $p \neq q$) and “weights” $v^m = \{v_1^m, \dots, v_m^m\} \subset \mathbb{C}$, and associated rational approximants

$$r^m(\omega) = \sum_{j=1}^m \frac{v_j^m f(\omega_j)}{\omega - \omega_j} \bigg/ \sum_{j=1}^m \frac{v_j^m}{\omega - \omega_j}. \quad (48)$$

Letting $\tilde{Z}_0 = \emptyset$, calling $\tilde{Z}_m := Z \setminus Z_m$, and using the enumeration $\tilde{Z}_m = \{\omega_1^m, \dots, \omega_{M-m}^m\}$, the inductive process proceeds by constructing the m -th support point

$$\omega_m = \operatorname{argmax}_{\omega \in \tilde{Z}_{m-1}} |r^{m-1}(\omega) - f(\omega)|,$$

setting $Z_m = Z_{m-1} \cup \{\omega_m\}$, and obtaining the m -th “weight vector” v^m as the solution of the least squares problem

$$v^m = \operatorname{argmin}_{v \in \mathbb{C}^m, \|v\|_m=1} \|A_m[f]v\|_{M-m}. \quad (49)$$

Here, for a positive integer n , $\|\cdot\|_n$ denotes the Euclidean norm in \mathbb{C}^n and $A_m[f]$ denotes the $(M-m) \times m$ Loewner matrix, whose (ij) entry is given by

$$(A_m[f])_{ij} = \frac{f(\omega_i^m) - f(\omega_j)}{\omega_i^m - \omega_j}.$$

(It is easy to check that the minimization problem (49) is equivalent to minimizing f times the denominator minus the numerator of the corresponding barycentric formulation (48) of the rational approximant; see [47, eq. 3.4]). Using the support points in the set Z_m and the weight vector v^m , the rational approximant r^m is constructed. The algorithm terminates when $\max_Z |r^m(\omega) - f(\omega)|$ is less than a user-specified error tolerance ε_{tol} . In practice the algorithm is terminated if $m = m_{\text{max}}$ for a suitably selected parameter m_{max} (usually $m_{\text{max}} = 100$). Meeting this stopping criterion before the user-prescribed tolerance ε_{tol} is achieved provides an indication that Z does not adequately represent f or that f has too many poles near the points in Z . In either cases the sample set should be adequately refined as is done e.g. as part of the adaptive algorithm described in Section 3.2.

A vector AAA algorithm, which produces a vector-valued rational approximant to a complex vector-valued function $\hat{f} : \mathbb{C} \rightarrow \mathbb{C}^N$, was introduced in [34]. As in the scalar case, the vector algorithm constructs a set of support points Z_m and a vector v^m of weights to produce a vector valued rational approximant $R^m(\omega) \approx \hat{f}(\omega)$. Analogous to the scalar case, the vector-valued rational approximant $R^m(\omega)$ is constructed inductively in the form of the quotient

$$R^m(\omega) = \sum_{j=1}^m \frac{v_j^m \hat{f}(\omega_j)}{\omega - \omega_j} \bigg/ \sum_{j=1}^m \frac{v_j^m}{\omega - \omega_j}. \quad (50)$$

Letting $\hat{f}_n(\omega), R_n^m(\omega), (1 \leq n \leq N)$ denote the components of \hat{f} and R^m respectively, the support points ω_m at each step are computed as

$$\omega_m = \operatorname{argmax}_{\omega \in \tilde{Z}_{m-1}, 1 \leq n \leq N} |R_n^{m-1}(\omega) - \hat{f}_n(\omega)|$$

To compute the weights a problem of the same form as (49) is solved, namely

$$v^m = \operatorname{argmin}_{v \in \mathbb{C}^m, \|v\|_m=1} \|B_m[\hat{f}]v\|_{N(M-m)}, \quad (51)$$

where $B_m[\hat{f}]$, is a block matrix given by $B_m[\hat{f}] = [A_m[\hat{f}_1] \dots A_m[\hat{f}_N]]^T$.

The least-squares problem in the set-valued AAA algorithm (51) becomes prohibitively expensive as N grows, even if an efficient implementation such as suggested in [34] is used. To address this issue a random sketching approach was recently proposed in [25], where for a random matrix $V \in \mathbb{C}^{N \times \ell}$ with $\ell \ll N$, the vector-valued AAA algorithm is applied to the function $\hat{g}(\omega) = V^T \hat{f}(\omega)$ to compute the rational approximant

$$R^m(\omega) = \sum_{j=1}^m \frac{v_j^m \hat{g}(\omega_j)}{\omega - \omega_j} \bigg/ \sum_{j=1}^m \frac{v_j^m}{\omega - \omega_j}. \quad (52)$$

A rational approximant for \hat{f} is then constructed by substituting the values $\hat{g}_\ell(\omega_j)$ by $\hat{f}(\omega_j)$ in equation (52). The numerical experiments and theoretical analysis in [25] show that even for small values of ℓ (e.g. $\ell = 2, 4, 8$) the random sketching rational approximation algorithm produces a highly accurate rational approximant.

The numerical implementations presented in this paper utilize the AAA and vector-AAA algorithms provided in [23] and [34], respectively. For the vector-AAA algorithm we have additionally implemented a spurious pole “clean up” algorithm based on the prescription given in [47].

Remark 4. The notation R^m and v_j^m used in this section for the AAA approximants and weights is useful due to the inductive nature of the AAA construction. However, this notation is not necessary for the practical use of the approximants. Therefore, in the remainder of the paper, we will omit it and instead express the AAA approximant produced by the algorithm without explicitly incorporating the numerator/denominator degree m (except in the upper summation limit):

$$R(\omega) = \sum_{j=1}^m \frac{v_j \hat{f}(\omega_j)}{\omega - \omega_j} \bigg/ \sum_{j=1}^m \frac{v_j}{\omega - \omega_j}. \quad (53)$$

3.2 Adaptive random-excitation (RE) resonance evaluation

To motivate the adaptive algorithm for evaluation of incidence-excited resonances presented in section 3.3, this section briefly reviews the adaptive algorithm [15, Algorithm 2] for evaluation of all resonances in a given domain in the complex plane, which is based on the use of random excitation (RE). The adaptive RE algorithm has proven effective for evaluation of complex resonances, even in presence of large numbers of resonances and/or high frequencies.

To evaluate the resonances associated with \mathcal{U}_ω (44), the RE method computes values of ω for which matrix-valued function \tilde{H}_ω (36) is not invertible by seeking poles of the randomly scalarized resolvent

$$s(\omega) = u^* \tilde{H}_\omega^{-1} v \quad \text{where} \quad u, v \in \mathbb{C}^N \quad \text{are fixed random vectors.}$$

This approach thus uses the matrix function’s resolvent \tilde{H}_ω^{-1} under random excitation vector v and random scalarization vector u , to produce the meromorphic function $s(\omega)$, whose poles coincide, with overwhelming probability, with the desired resonant values of \tilde{H}_ω [15]. To compute the poles of $s(\omega)$ (and, thus, the resonances of \tilde{H}_ω) contained within a set $D \subset \mathbb{C}$ and its boundary, the RE method utilizes the AAA algorithm to obtain the rational approximant $r^m(\omega) \approx s(\omega)$ using points along the boundary of D . This approximant is useful in that, provided the set D is “sufficiently small” and an adequate number of roughly equispaced sampling points are used along the boundary of D , the poles of $r^m(\omega)$ within D provide close approximations of the poles of $s(\omega)$. In order to tackle the generic case in which a proposed set D may not be sufficiently small, the RE method employs an adaptive search technique by partitioning D into sub-regions and computing the poles within each subregion, typically using rectangular domains D which are subsequently dyadically partitioned, in an iterative fashion, into smaller rectangular subregions—as detailed in [15]. The algorithm terminates when no new poles are found in each subregion, upon which a certain secant method-based termination stage is used to significantly enhance accuracy and to filter out spurious poles that may (rarely) be produced by the AAA algorithm.

3.3 Incidence-excitation (IE) resonance evaluation for time-domain problems

The complex resonances most relevant to the FTH method reviewed in Section 2.1 are those whose real parts lie within the incident-field interval I (12), which are located near the real axis, and whose residue is not numerically insignificant. Indeed, such complex resonances lead to sharp spikes in $U_k^{\text{slow}}(\mathbf{r}, \omega)$ along the real frequency axis, as illustrated by the numerical experiments in Section 6.3, and, therefore, the accurate

evaluation of the Fourier transform (15) often requires the use of extremely fine integration meshes. In order to avoid this difficulty a certain complex resonance singularity subtraction technique is proposed in Section 4, which, in particular requires as input the positions and residues of all relevant near-real complex resonances. This section presents the “Incident Excitation” (IE) algorithm which, in contrast with the RE algorithm presented in the previous section (which obtains complex resonances ω within a given region in the complex plane on the basis of the scalarization of the resolvent \tilde{H}_ω^{-1} via pre- and post-multiplication by a pair of *random* vectors at a number of frequencies ω in the *complex* plane) aims to compute all complex resonances responsible for the spikes in $U_k^{\text{slow}}(\mathbf{r}, \omega)$ on the sole basis of the action of the discrete version \tilde{H}_ω^{-1} of the resolvent H_ω^{-1} on *incident field data* (5) (eqs. (36)-(38)) at *real* frequencies ω —where either $H_\omega = C_{\omega, \eta}$ or $H_\omega = S_\omega$ (equations (21) and (26)), as applicable.

To introduce the IE algorithm we first observe that, in view of (31), (33) and (34) together with (18) or (27), as applicable, the complex resonances of $U_k^{\text{slow}}(\mathbf{r}, \omega)$ coincide with the complex poles of $U_{\mathbf{p}}(\mathbf{r}, \omega)$, and thus, with the complex poles of $\psi_{\mathbf{p}}(\mathbf{r}', \omega) = (H_\omega^{-1} B_{\mathbf{p}}(\cdot, \omega))(\mathbf{r}, \omega)$ (which therefore are, in particular, independent of both \mathbf{r} and k). The IE algorithm thus seeks to evaluate all complex poles of the incidence-excited resolvent (IE)

$$(H_\omega^{-1} B_{\mathbf{p}}(\cdot, \omega))(\mathbf{r}, \omega) \quad (54)$$

in the box

$$\mathcal{M}_h^I := \{\omega \in \mathbb{C} \mid \text{Re}(\omega) \in I, \text{Im}(\omega) \in [-h, 0]\} \quad \text{for some prescribed parameter } h > 0, \quad (55)$$

and associated residues. Using the enumeration ρ_n and $c_{\mathbf{p}, n}(\mathbf{r})$ ($1 \leq n \leq N_h(I)$) of all such resonances and residues and considering (33), we have

$$c_{\mathbf{p}, n}(\mathbf{r}) = \frac{1}{2\pi i} \int_{C_n} U_{\mathbf{p}}(\mathbf{r}, \omega) d\omega, \quad 1 \leq n \leq N_h(I), \quad (56)$$

where C_n is a contour which encloses ρ_n and no other complex resonances.

It is important to note that, in view of (31) and (33), the residues $c_{\mathbf{p}, n}(\mathbf{r})$ may be expressed in terms of the density residues

$$\hat{c}_{\mathbf{p}, n}(\mathbf{r}') = \frac{1}{2\pi i} \int_{C_n} \psi_{\mathbf{p}}(\mathbf{r}', \omega) d\omega, \quad \mathbf{r} \in \Gamma. \quad (57)$$

Indeed, on account of Remark 3 we have $\hat{c}_{\mathbf{p}, n}(\mathbf{r}) = \lim_{\omega \rightarrow \rho_n} (\omega - \rho_n) \psi_{\mathbf{p}}(\mathbf{r}, \omega)$. Thus, using the single-layer and combined-field field representations \mathcal{S}_ω and $\mathcal{C}_{\omega, \eta}$ (equations (27) and (18), respectively) with $\omega = \rho_n$, together with the dominated convergence theorem, we obtain

$$c_{\mathbf{p}, n}(\mathbf{r}) = \mathcal{S}_{\rho_n}^{\text{arc}}[\hat{c}_{\mathbf{p}, n}](\mathbf{r}) \quad \text{or} \quad c_{\mathbf{p}, n}(\mathbf{r}) = \mathcal{C}_{\rho_n, \eta}[\hat{c}_{\mathbf{p}, n}](\mathbf{r}) \quad \mathbf{r} \in \Omega^e, \quad \text{as applicable} \quad (58)$$

in the open and closed curve cases, respectively.

Utilizing the Cauchy–Schwarz inequality we obtain

$$|c_{\mathbf{p}, n}(\mathbf{r})| \leq M_{\mathcal{S}}(\mathbf{r}) \|\hat{c}_{\mathbf{p}, n}(\mathbf{r}')\|_{L^2(\Gamma)} \quad \text{and} \quad |c_{\mathbf{p}, n}(\mathbf{r})| \leq M_{\mathcal{C}}(\mathbf{r}) \|\hat{c}_{\mathbf{p}, n}(\mathbf{r}')\|_{L^2(\Gamma)} \quad (59)$$

where, letting $\|\cdot\|_{L^2(\Gamma)}$ denote the L^2 norm on the curve Γ , we have set

$$M_{\mathcal{S}}(\mathbf{r}) = \|G_{\rho_n}(\mathbf{r}, \cdot)\|_{L^2(\Gamma)} \quad \text{and} \quad M_{\mathcal{C}}(\mathbf{r}) = \left\| \frac{\partial G_{\rho_n}(\mathbf{r}, \cdot)}{\partial n} - i\eta G_{\rho_n}(\mathbf{r}, \cdot) \right\|_{L^2(\Gamma)}.$$

This tells us that a given \mathbf{r} -dependent resonance $(\rho_n, c_{\mathbf{p}, n}(\mathbf{r}))$ can be neglected provided the corresponding \mathbf{r} -independent resonance $(\rho_n, \hat{c}_{\mathbf{p}, n})$ itself gives rise to negligible values of the quantity $\hat{c}_{\mathbf{p}, n}/(\omega - \rho_n)$ for ω along the interval I .

In short, the complex resonances ρ_n which cause spikes in $U_k^{\text{slow}}(\mathbf{r}, \omega)$ are the complex resonances near the real axis whose density residue $\hat{c}_{\mathbf{p},n}(\mathbf{r}')$ is not negligible. In order to produce all such resonances the proposed IE method resorts to computing a rational approximant to $\psi_{\mathbf{p}}(\mathbf{r}', \omega)$ by means of the random sketching algorithm described in Section 3.1. Unfortunately, however, a direct application of the random sketching approach to the complete interval I generally fails to determine all relevant resonance pairs $(\rho_n, \hat{c}_{\mathbf{p},n})$. In order to tackle this difficulty an adaptive approach (analogous to but different from the one utilized by RE method) is proposed in Section 3.3.1 for the evaluation of the IE pole locations ρ_n . Section 3.3.2 then describes a method to compute the corresponding residues $c_{\mathbf{p},n}$ (56) by re-using the rational approximants to $\psi_{\mathbf{p}}(\mathbf{r}, \omega)$ that are generated as part of by the adaptive IE-based pole-search algorithm.

3.3.1 Adaptive IE resonance evaluation

For a given incident field whose frequency content vanishes outside an interval $I = [W_1, W_2]$ (so that, e.g., in the context set up in Section 2.1, $B(\omega) = 0$ for $\omega \notin I$) the adaptive IE method seeks the set P_h^I of IE complex resonances in the box (55), for some prescribed parameter $h > 0$, on the basis of the discrete version

$$\hat{f}(\omega) = (\hat{f}_1(\omega), \dots, \hat{f}_N(\omega)) = (\tilde{\psi}_{\mathbf{p},1}(\omega), \dots, \tilde{\psi}_{\mathbf{p},N}(\omega)) = \tilde{\psi}_{\mathbf{p}}(\omega) \quad (60)$$

(equation (38)) of the density solutions $\psi_{\mathbf{p}}(\cdot, \omega) = (H_\omega)^{-1} B_{\mathbf{p}}(\cdot, \omega)$, with ω in a discrete set of (generally non-equispaced) adaptively-selected frequencies within the interval I , as described in what follows. (The set P_h^I then serves as the input to the singularity subtraction algorithm introduced in Section 4.)

Algorithm 1: Adaptive Incidence-Excited Resonance Evaluation

Input: An interval $I = [W_1, W_2]$, a number J of frequencies to use in each interval, AAA stopping parameters m_{\max} and ε_{tol} , and singularity-box depth $h > 0$.

```

1 Function reallineadaptive( $I, J$ )
2   Evaluate  $\tilde{\psi}_p$  (60) at  $J$  equally spaced frequencies in the interval  $I$ .
3   Compute a rational approximant  $R(\omega)$  of the incidence-excited resolvent (61) evaluated by the
      random sketching algorithm applied to the values  $\tilde{\psi}_p$  computed at the previous step.
4   if the random sketching error converged within  $\varepsilon_{\text{tol}}$  then
5     Set  $R^I(\omega) = R(\omega)$  and compute  $P_h^I$ .
6     return  $R^I(\omega), P_h^I$ .
7   else
8     Compute the midpoint  $W_3 = (W_2 + W_1)/2$ , and set  $I_{\text{left}} = [W_1, W_3]$  and  $I_{\text{right}} = [W_3, W_2]$ .
9     return reallineadaptive( $I_{\text{left}}, J$ ) and reallineadaptive( $I_{\text{right}}, J$ )
10  end
11 end

```

In detail, starting with a set $\mathcal{F} = \{\omega_1, \dots, \omega_J\}$ of J equispaced frequencies in the interval I , the IE algorithm first seeks to compute a vector-valued rational approximant $R(\omega) = R^m(\omega)$ of the vector

$$\tilde{H}_\omega^{-1} \tilde{B}_{\mathbf{p}}(\omega), \text{ on the basis of its values for } \omega \in \mathcal{F}, \quad (61)$$

by applying the random sketching method for vector-valued functions of ω which is described in Section 3.1. (Per Remark 4 the superindex m in the notation for the rational approximant $R = R^m$ is suppressed here and in what follows.) If the random sketching method converges within the prescribed error tolerance ε_{tol} for some value of $m \leq m_{\max}$, then the algorithm is completed in its $L = 1$ step by setting $L = 1$, $I_L = I_1 = I$, $\mathcal{F}_L = \mathcal{F}_1 = \mathcal{F}$, $R^{I_L} = R^{I_1} = R$, and by producing the set $P_h^I = P_h^{I_1}$ that comprises all poles of $R^{I_1}(\omega)$ contained in $\mathcal{M}_h^{I_1}$ (55). Otherwise the interval I is divided at the midpoint $W_3 = (W_2 + W_1)/2$ into two subintervals $I_{\text{left}} = [W_1, W_3]$ and $I_{\text{right}} = [W_3, W_2]$, and the same procedure is applied to the intervals

I_{left} and I_{right} , using a set of J equispaced frequencies in each case, increasing the index L by 1 each time the random sketching method converges within the error tolerance ε_{tol} for some value of $m \leq m_{\text{max}}$ and for some subinterval $I_L \subset I$, and producing, upon each such completion, the corresponding interval I_L , rational approximant R^{I_L} , set $P_h^{I_L}$ of poles of R^{I_L} in the box $\mathcal{M}_h^{I_L}$, and it proceeds by applying the same procedure to the interval I_{right} . The process terminates when the random sketching method has converged, within the tolerance ε_{tol} and for some value of $m \leq m_{\text{max}}$, on every subinterval in a partition I_1, \dots, I_L of the interval I :

$$I = \bigcup_{\ell=1}^L I_\ell. \quad (62)$$

Thus, upon completion, the IE algorithm results in a partition I_1, \dots, I_L of I , a set of rational approximants

$$R^{I_1}, \dots, R^{I_L} \quad (63)$$

applicable over the corresponding sets $\mathcal{M}_h^{I_1}, \dots, \mathcal{M}_h^{I_L}$, respectively, and associated sets of poles $P_h^{I_1} \subset \mathcal{M}_h^{I_1}, \dots, P_h^{I_L} \subset \mathcal{M}_h^{I_L}$. The set of all poles obtained, in particular, is given by

$$P_h^I = \bigcup_{\ell=1}^L P_h^{I_\ell} \subset \mathcal{M}_h^I. \quad (64)$$

A pseudocode description of the method is presented in Algorithm 1.

On the basis of a broad set of numerical experiments we have found that using the parameters $m_{\text{max}} = 100$, AAA tolerance $\varepsilon_{\text{tol}} = 10^{-10}$, with $J \in [200, 400]$ in each relevant interval, Algorithm 1 is effective at capturing all relevant resonances associated with the interval I . For computational efficiency, values of (61) computed on each level of the recursion can be stored and used in subsequent levels. It has also been observed that the choice of the parameter $h \in [0.2, 0.5]$ allows the set P_h^I to serve as adequate input to the singularity subtraction algorithm introduced in Section 4, without capturing false poles of the rational approximant which are far from the real axis. Additionally, in situations for which only a low number of integral equation inversions are to be used, (say less than 200), we have found that it is preferable to use Algorithm 1 without adaptive steps (resulting in a rational approximant with degree $m \leq m_{\text{max}} = J/2$ (cf. [47, sec. 3])), rather than using a smaller value of J (such as e.g. $J = 20$) and applying the full adaptive algorithm with a large value of the tolerance ε_{tol} . Section 6.2 demonstrates the effectiveness of the overall algorithm, and it analyzes both the accuracy of the computed resonances and the significance—or lack thereof—of any resonances not captured by the method for a given value of h .

Remark 5. The application of Algorithm 1 can become expensive in presence of a large number of IE resonances with real parts in the interval I —since, in such cases, many adaptive steps may be required. The algorithm could alternatively be applied to subintervals forming a partition of I , but the selection of such partition presents a difficulty, in principle—since the number of relevant complex resonances in any given subinterval of I is not known a priori. A more general “sampling” algorithm has therefore been devised in which the interval I is *sampled* by means of a small number of small subintervals on which Algorithm 1 can be cheaply applied, and thus produce useful estimates of the variation of the density of IE resonances with real part in the interval I . Using such estimates, a partition (62) of adequately varying sizes may be produced such that the application of Algorithm 1 on I_j with $m_{\text{max}} = 100$ produces all the resonances relevant to I_j . A complete exploration and demonstration of the sampling algorithm is beyond the scope of this paper, however, and is left for future work.

3.3.2 Computation of residues (56)

Once the set (64) of IE complex resonances has been obtained, the corresponding spatially dependent residues $c_{\mathbf{p},n}(\mathbf{r})$ can be computed using (57)–(58), where, as in Section 3.3, the enumeration ρ_n ($1 \leq n \leq$

$N_h(I)$) of the set P_h^I is employed. Evaluating the expression (57) for $\widehat{c}_{\mathbf{p},n}(\mathbf{r}')$ requires knowledge of the density solution $\psi_{\mathbf{p}}(\mathbf{r}', \omega)$ in (31) for a sufficient number of values of $\omega \in C_n$ and for all values of \mathbf{r}' in the discretization used for the boundary Γ . (For all of the numerical examples presented in this paper, the contour C_n was taken to be a circle centered at the numerical approximation of the corresponding complex resonance, with radius 10^{-5} , and the necessary integrals around C_n were evaluated using the trapezoidal rule applied to (57) with a number $J_C = 10$ of integration points $\omega_1, \dots, \omega_{J_C}$.) To avoid the costly inversion of boundary integral operators around poles ρ_n with $1 \leq n \leq N_h(I)$ and for frequencies ω_j with $1 \leq j \leq J_C$, the densities $\psi_{\mathbf{p}}(\mathbf{r}', \omega_j)$ are obtained from the rational approximants produced as part of the IE algorithm's resonance evaluation. Specifically, for $\rho_n \in P_h^{I_\ell}$, the corresponding IE rational approximant R^{I_ℓ} is used. Thus, for each $1 \leq j \leq J_C$, an accurate numerical approximation of $\psi_{\mathbf{p}}(\mathbf{r}', \omega_j)$ is obtained by exploiting the relation

$$\psi_{\mathbf{p}}(\mathbf{r}', \omega_j) \approx R^{I_\ell}(\omega_j), \quad (65)$$

which allows the integral (56) to be evaluated without the need for additional boundary integral operator inversions. Note the implicit \mathbf{r}' dependence of the right-hand side in (65) per equation (53) together with (38) and (60).

4 Frequency-domain singularity subtraction

While the FTH method reviewed in Section 2.1 allows for dispersionless simulation of (1) for arbitrarily long times, a difficulty arises when complex resonances lie near the real axis, namely the integrand of the inverse Fourier transform (15) becomes near-singular. This leads to slow convergence of the Fourier transform method reviewed in Section 2.3—as it would indeed for any Fourier transform method which does not resolve the near singularities. This problem may be exacerbated for wideband or high-frequency problems and strongly trapping obstacles, where hundreds or thousands of poles may exist near the real axis. Section 4.1 introduces a complex resonance subtraction method that resolves this difficulty. Section 4.2 then establishes a technique for evaluation of the integrals related to the resonance subtraction, and finally Section 4.3 discusses the relationship of that technique to asymptotic expansions of $u(\mathbf{r}, t)$.

4.1 Singularity subtraction

In order to improve the convergence of the numerical evaluation of the inverse Fourier transform (15) in the presence of complex resonances near the real axis the method first evaluates all such nearly-real complex resonances via the IE algorithm introduced in Section 3.3. Since $u_k(\mathbf{r}, t)$ is produced from $U_k^{\text{slow}}(\mathbf{r}, \omega)$, in view of (34) we see that the poles of $U_{\mathbf{p}}(\mathbf{r}, \omega)$ and corresponding residues account for all of the near singular behavior in the integrand of (15).

In detail, with reference to equations (56) and (64), and with I as defined in (12), we use all complex resonances $\rho_n \in P_h^I$ for $1 \leq n \leq N_h(I)$, together with their corresponding residues $c_{\mathbf{p},n}(\mathbf{r})$, to define the regularized function $U_{\mathbf{p},h}^s(\mathbf{r}, \omega)$ via singularity subtraction:

$$U_{\mathbf{p},h}^s(\mathbf{r}, \omega) = U_{\mathbf{p}}(\mathbf{r}, \omega) - \sum_{n=1}^{N_h(I)} \frac{c_{\mathbf{p},n}(\mathbf{r})}{\omega - \rho_n}. \quad (66)$$

In view of (34), the regular part of the Fourier transform (15) is then defined by

$$\mathcal{I}_{1,k}(\mathbf{r}, t) = \frac{1}{2\pi} \int_{W_1}^{W_2} A_k^{\text{slow}}(\omega) U_{\mathbf{p},h}^s(\mathbf{r}, \omega) e^{-i\omega(t-s_k)} d\omega, \quad (67)$$

and, thus, letting the “singularity integrals” be given by

$$\mathcal{I}_{2,k}(\mathbf{r}, t) = \frac{1}{2\pi} \sum_{n=1}^{N_h(I)} c_{\mathbf{p},n}(\mathbf{r}) \int_{W_1}^{W_2} \frac{A_k^{\text{slow}}(\omega)}{\omega - \rho_n} e^{-i\omega(t-s_k)} d\omega, \quad (68)$$

we may re-express (15) in the form

$$u_k^I(\mathbf{r}, t) = \mathcal{I}_{1,k}(\mathbf{r}, t) + \mathcal{I}_{2,k}(\mathbf{r}, t). \quad (69)$$

Therefore, the field $u^I(\mathbf{r}, t)$ in (16) is given by

$$u^I(\mathbf{r}, t) = \mathcal{I}_1(\mathbf{r}, t) + \mathcal{I}_2(\mathbf{r}, t). \quad (70)$$

where

$$\mathcal{I}_1(\mathbf{r}, t) = \sum_{k=1}^K \mathcal{I}_{1,k}(\mathbf{r}, t) \quad \text{and} \quad \mathcal{I}_2(\mathbf{r}, t) = \sum_{k=1}^K \mathcal{I}_{2,k}(\mathbf{r}, t). \quad (71)$$

Utilizing (8) and (9), further, the integral \mathcal{I}_2 becomes

$$\mathcal{I}_2(\mathbf{r}, t) = \frac{1}{2\pi} \sum_{n=1}^{N_h(I)} c_{\mathbf{p},n}(\mathbf{r}) \int_{W_1}^{W_2} \frac{A(\omega)}{\omega - \rho_n} e^{-i\omega t} d\omega. \quad (72)$$

The regular-part integrals $\mathcal{I}_{1,k}(\mathbf{r}, t)$ do not contain the spikes induced by the singularities $(\rho_n, c_{\mathbf{p},n}(\mathbf{r}))$, and may therefore be integrated effectively using the FTH quadrature scheme described in Section 2.3. Turning to the integrals $\mathcal{I}_2(\mathbf{r}, t)$ in (72), we note that, unlike A_k^{slow} , the function A in (72) is not slowly oscillatory. However, this does not hinder the evaluation of the integrals in that equation, which—being independent of both k and \mathbf{r} —can be computed rapidly using a numerical algorithm, described in the following section, that combines an exponentially convergent large-time asymptotic expansion with numerical quadrature at pre-asymptotic times.

4.2 Evaluation of the singularity integral $\mathcal{I}_2(\mathbf{r}, t)$

To evaluate $\mathcal{I}_2(\mathbf{r}, t)$ it suffices to compute the \mathbf{r} -independent integrals

$$\int_{W_1}^{W_2} \frac{A(\omega)}{\omega - \rho_n} e^{-i\omega t} d\omega \quad (73)$$

which appear on the right-hand side of (72). As suggested in the previous section and detailed below in the present section, for large times this integral can be obtained on the basis of an asymptotic expansion. Taking into account the proximity of ρ_n to the real axis, on the other hand, to evaluate the integral numerically at pre-asymptotic times we rewrite it in the form

$$\int_{W_1}^{W_2} \frac{A(\omega)}{\omega - \rho_n} e^{-i\omega t} d\omega = \int_{W_1}^{W_2} \frac{A(\omega)e^{-i\omega t} - A(\rho_n)e^{-i\rho_n t}}{\omega - \rho_n} d\omega + A(\rho_n)e^{-i\rho_n t} \int_{W_1}^{W_2} \frac{1}{\omega - \rho_n} d\omega. \quad (74)$$

The first right-hand integrand in (74) is smooth, and it can therefore be effectively tackled, for t small enough, by means of standard quadrature methods; in this paper we employ the Clenshaw-Curtis rule [55]. The second integral, in turn, can be evaluated analytically: it equals $\log \frac{W_2 - \rho_n}{W_1 - \rho_n}$.

For large times, the integrands in (73) and (74) become highly oscillatory functions of ω , rendering standard quadrature methods ineffective. As suggested above, we instead employ an asymptotic expansion derived by deforming the integration contour in (73) onto the remaining three sides of the boundary of \mathcal{M}_h^I

(eq. (55)): C_1 which goes from W_2 to $W_2 - hi$, C_2 which goes from $W_2 - hi$ to $W_1 - hi$, and C_3 which goes from $W_1 - hi$ to W_1 ; without loss of generality, it is assumed that none of the poles in P_h^I (64) lies on the curves C_j ($1 \leq j \leq 3$). In view of the residue theorem we obtain

$$\int_{W_1}^{W_2} \frac{A(\omega)}{\omega - \rho_n} e^{-i\omega t} d\omega = -2\pi i A(\rho_n) e^{i\rho_n t} + \sum_{j=1}^3 \int_{C_j} \frac{A(\omega)}{\omega - \rho_n} e^{-i\omega t} d\omega. \quad (75)$$

To estimate the contribution from each segment C_j we write $\omega = \omega_1 + i\omega_2$, and in view of (4), we re-express $A(\omega)$ in the form

$$A(\omega) = \int_0^{T^{\text{inc}}} a(t) e^{i\omega_1 t - \omega_2 t} dt = e^{-\omega_2 T^{\text{inc}}} A^{\text{bd}}(\omega) \quad \text{with} \quad A^{\text{bd}}(\omega) = \int_0^{T^{\text{inc}}} a(t) e^{i\omega_1 t - \omega_2(t - T^{\text{inc}})} dt$$

—where, for the relevant values $\omega_2 \leq 0$ of $\omega_2 = \text{Im}(\omega)$, the bounded version A^{bd} of A satisfies $|A^{\text{bd}}(\omega)| \leq \int_0^{T^{\text{inc}}} |a(t)| dt$. The integral (73) along the contour C_j ($j = 1, 2, 3$) may be re-expressed in the form

$$\int_{C_j} \frac{A(\omega)}{\omega - \rho_n} e^{-i\omega t} d\omega = \int_{C_j} e^{\omega_2(t - T^{\text{inc}})} \frac{A^{\text{bd}}(\omega_1 + i\omega_2)}{\omega_1 + i\omega_2 - \rho_n} e^{-i\omega_1 t} d\omega. \quad (76)$$

In particular, for $j = 2$ we have $\omega_2 = -h < 0$, and, thus

$$\left| \int_{C_2} \frac{A(\omega)}{\omega - \rho_n} e^{-i\omega t} d\omega \right| \leq M_2 e^{-h(t - T^{\text{inc}})} \quad (77)$$

for some constant $M_2 > 0$. In other words, the C_2 contribution decays exponentially fast for times $t > T^{\text{inc}}$. To estimate the integrals over C_j with $j = 1$ and $j = 3$, in turn, we first integrate by parts the integral A^{bd} , which yields

$$|A^{\text{bd}}(\omega_1 + i\omega_2)| \leq \frac{1}{|\omega_1 + i\omega_2|^n} \int_0^{T^{\text{inc}}} |a^{(n)}(t) e^{-\omega_2(t - T^{\text{inc}})}| dt \leq \frac{1}{|\omega_1|^n} \int_0^{T^{\text{inc}}} |a^{(n)}(t)| dt \quad \text{for all } \omega_2 \leq 0, \quad (78)$$

and, thus, for any given $\varepsilon^I > 0$ (cf. equations (12) and (13)), we have

$$|A^{\text{bd}}(W_1 + i\omega_2)| < \varepsilon^I \quad \text{and} \quad |A^{\text{bd}}(W_2 + i\omega_2)| < \varepsilon^I \quad \text{for all } \omega_2 \leq 0, \quad (79)$$

provided $W_2 > 0$ and $W_1 < 0$ are sufficiently large. Combining (76) and (79) shows that the contributions from the vertical contours C_1 and C_3 is a quantity of order $O(\varepsilon^I)$ for times $t > T^{\text{inc}}$, and, thus, in view of (72), and (75) we see

$$\mathcal{I}_2(\mathbf{r}, t) \sim - \sum_{n=1}^{N_h(I)} i c_{\mathbf{p},n}(\mathbf{r}) A(\rho_n) e^{-i\rho_n t} + O(e^{-h(t - T^{\text{inc}})}) + O(\varepsilon^I) \quad \text{as } t \rightarrow \infty. \quad (80)$$

For a related example which often arises in practice, and will be used in the numerical experiments, we consider the explicit case when $A(\omega) = \exp \frac{-(\omega - \omega_0)^2}{\sigma^2}$. Again letting $\omega = \omega_1 + i\omega_2$ the integral (73) evaluated along the same contours C_j , ($j = 1, 2, 3$) is expressed in the form

$$\int_{C_j} \exp \left(\frac{-(\omega_1 - \omega_0)^2 + \omega_2^2}{\sigma^2} + \omega_2 t \right) \frac{\exp(2i(\omega_1 \omega_0 - \omega_2 \omega_0) - i\omega_1 t)}{\omega_1 + i\omega_2 - \rho_n} d\omega, \quad j = 1, 2, 3.$$

The contribution from C_2 , for which $\omega_2 = h$, is exponentially small, decaying at the rate of $e^{-h(t - h/\sigma^2)}$ after time $t = h/\sigma^2$, so that

$$\mathcal{I}_2(\mathbf{r}, t) \sim - \sum_{n=1}^{N_h(I)} i c_{\mathbf{p},n}(\mathbf{r}) A(\rho_n) e^{-i\rho_n t} + O(e^{-h(t - h/\sigma^2)}) + O(\varepsilon^I) \quad \text{as } t \rightarrow \infty. \quad (81)$$

where $\varepsilon^I = A(W_1) = A(W_2)$ accounts for the contributions from the vertical contours C_1 and C_3 .

4.3 Time-domain singularity expansion

The asymptotic expansion of $\mathcal{I}_2(\mathbf{r}, t)$ in (80) is closely related to asymptotic expansions

$$u(\mathbf{r}, t) \sim \sum_{n=1}^{\infty} -i c_{\mathbf{p}, n}(\mathbf{r}) A(\rho_n) e^{-i \rho_n t} \quad \text{as } t \rightarrow \infty, \quad (82)$$

of the scattered field $u(\mathbf{r}, t)$ (where ρ_n ranges over all complex resonances) that have been widely used in the literature [9, 27, 38, 41, 42]; the overall approach has come to be known as the “Singularity Expansion Method” [9].

The validity of such an expansion (which in the context of Sections 4.1 and 4.2, amounts to exponential decay of the quantity \mathcal{I}_1 in (71), has only been established [32, 33, 39, 52] for 3D non-trapping scatterers (for which a billiard ball bouncing off the scatterer boundaries escapes to infinity after finitely many bounces). In two dimensions such an expansion could only hold provided the frequency content of the incident excitation tends to vanish sufficiently rapidly as the frequency ω tends to zero—since, as it is known [46], 2D scattered field only decay as $O(1/(t \log^2(t)))$ in presence of zero frequency content. Although no proofs have been presented for the 2D case, we conjecture that the proof strategy used in [4] could establish the validity of such an expansion—up to an arbitrarily small error ε^I (cf. (80))—for scatterers satisfying a certain “ q -growth condition” on the resolvent of the Green’s function operator. This condition is met by a broad class of scatterers, including highly trapping ones.

Additionally, a wide range numerical tests presented in [5] as well as Section 6 below provide strong evidence of the validity of the asymptotic expansion (82) even for very highly trapping scatterers—where, as illustrated on the right panel in Figure 2, 2D-decay up to the intensity level induced by the zero-frequency content takes place, and where full exponential decay occurs, certainly for 3D configuration independently of the existence of zero-frequency content, and even in 2D, provided the frequency content of the incident excitation vanishes in a neighborhood of $\omega = 0$.

5 Numerical implementation of FTH with Singularity Subtraction

This section presents the proposed Singularity Subtraction-enabled FTH algorithm (FTH-SS) for the numerical solution of the initial and boundary-value problem (1). This method, which combines the FTH methodology reviewed in Section 2.1 with the singularity subtraction strategy embodied in equations (66)–(70) and (80), proceeds by first computing the incidence-excited complex resonances and their residues by means of the IE method (Section 3.3), and then obtaining $u \approx u^I(\mathbf{r}, t)$ on the basis of (70).

To reduce computational costs, the algorithm obtains the densities $\psi_{\mathbf{p}}$ (that, per equations (31)–(34) and (11)–(15), are needed by the FTH algorithm to compute the solutions U_k^{slow}), by means of an inexpensive reprocessing step applied to the densities $\psi_{\mathbf{p}}$ (eq. (31)) generated by Algorithm 1 as part of the evaluation of IE resonances. While the frequency set \mathcal{F}_L produced upon completion of Algorithm (1) generally differs from the frequency set \mathcal{F} (30) needed to compute the inverse Fourier-transform by the quadrature rules described in Section 2.3, however $\mathcal{D}_{\mathcal{F}}$ (32) may be cheaply computed using the rational approximants (63). Indeed, considering the partition (62), for $\omega \in \mathcal{F} \cap I_\ell$ ($\ell = 1, \dots, L$) the approximant $R^{I_\ell}(\omega_j)$ provides the necessary (accurate) approximations

$$\psi_{\mathbf{p}}(\mathbf{r}', \omega) \approx R^{I_\ell}(\omega), \quad \omega \in \mathcal{F} \cap I_\ell. \quad (83)$$

Once the set $\mathcal{D}_{\mathcal{F}}$ has been obtained, the integral $\mathcal{I}_1(\mathbf{r}, t)$ is evaluated by means of (71) using the quadrature rules presented in Section 2.3. The evaluation of $\mathcal{I}_2(\mathbf{r}, t)$ proceeds under two different scenarios. At pre-asymptotic times, on one hand, this integral is obtained using (72) and (74) by following the description accompanying the latter equation. For sufficiently large times the asymptotics described in Section 4.2 are used instead, leading to significant computing-time savings (as evaluation of integrals with

highly-oscillatory integrands is avoided) while capturing exponential solution decay that, however, for highly trapping structures, can continue to produce significant scattered fields for long times—as illustrated in Figures 11 and 12. A pseudo-code for the singularity subtraction method, provided in Algorithm 2, evaluates the approximation (16) $u^I(\mathbf{r}, t)$ of $u(\mathbf{r}, t)$ for all \mathbf{r} in a given set \mathbf{R} of spatial observation points at which the scattered field is to be produced.

Algorithm 2: Singularity subtraction-enabled FTH algorithm (FTH-SS)

- 1 Compute the set of rational approximants (63) and corresponding poles P_h^I relevant to the incident field using Algorithm 1.
 - 2 For each pole in P_h^I compute the residues at all points in \mathbf{R} using the method in Section 3.3.2.
 - 3 For the equally spaced discrete set of frequencies \mathcal{F} (30), compute the set of densities $\mathcal{D}_{\mathcal{F}}$ using the rational approximants (63).
 - 4 Using $\mathcal{D}_{\mathcal{F}}$ evaluate $U_{\mathbf{p}}(\mathbf{r}, \omega)$ for all frequencies in \mathcal{F} and all points in \mathbf{R} .
 - 5 Compute the singularity-subtracted version $U_{\mathbf{p},h}^s(\mathbf{r}, \omega)$ (66) of $U_{\mathbf{p}}$
 - 6 Evaluate $u^I(\mathbf{r}, t) = \mathcal{I}_1(\mathbf{r}, t) + \mathcal{I}_2(\mathbf{r}, t)$ (70) using by the quadrature rules discussed in Section 2.3 for \mathcal{I}_1 and the quadrature and asymptotic expansion methods discussed in Section 4.2 for \mathcal{I}_2 .
-

6 Numerical results

This section presents a variety of numerical illustrations of the FTH-SS algorithm and its various elements, including illustrations of the exponential convergence of the asymptotic expansions (80) and (81), demonstrations of the ability of the IE method to regularize Fourier-transform integrals via singularity subtraction, as well as applications of the overall FTH-SS method in challenging configurations containing trapping obstacles. The examples considered include test cases for both open-arc and closed-curve scatterers, such as those shown in Figure 1, along with a closed circular geometry and the whispering-gallery configuration depicted in Figure 11.

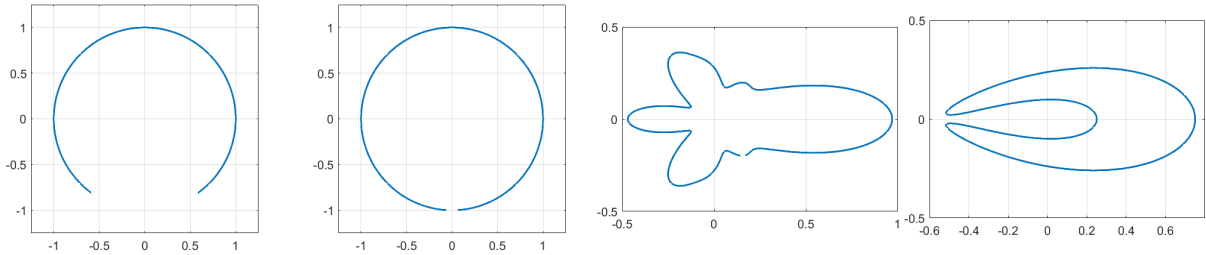


Figure 1: Several scatterers used in the examples as discussed in the text. From left to right: circular arc with opening 1.25 radians, circular arc with opening 0.125 radians, open rocket shaped cavity, closed cavity.

The first two panels in Figure 1 consist of circular arcs of radius 1 with apertures spanning 1.25 radians and 0.125 radians, respectively. The rocket-shaped in the third panel, is given by the parametrization $\gamma : [0, 2\pi] \rightarrow \mathbb{R}^2$ given by $\gamma(s) = (C(s) \cos(s), C(s) \sin(s))$ where

$$C(s) = 0.35 + 0.1 \cos(s) + 0.12 \cos(2s) + 0.15 \cos(3s) + 0.1 \cos(4s) + 0.1 \cos(6s) + 0.05 \cos(8s).$$

The full (closed) rocket boundary is produced when the full span $0 \leq s \leq 2\pi$ is used, while the rocket-with-opening displayed in Figure 1 is obtained by restricting the parametrization to the complement of the interval $5.338 \leq s \leq 5.427$. The closed-curve cavity presented in the fourth panel, finally, coincides with the one given in [22, Fig. 1].

Two incident fields, $u_1^{\text{inc}}(\mathbf{r}, t)$ and $u_2^{\text{inc}}(\mathbf{r}, t)$ (see equation (2)), are considered in this section. The first is defined by

$$u_1^{\text{inc}}(\mathbf{r}, t) = \text{Fourier transform of } e^{-\frac{(\omega-\omega_0)^2}{\sigma^2}}, e^{i\kappa(\omega)\mathbf{p}\cdot\mathbf{r}}, \quad (84)$$

for various choices of the parameters \mathbf{p} , ω_0 , and σ . The second incident field uses the chirp function

$$a(t) = \sin\left(g(t) + \frac{1}{4000}g^2(t)\right), \quad \text{where } g(t) = 4t + 6\cos\left(\frac{t}{\sqrt{12}}\right), \quad (85)$$

combined with the window function (7) and given parameters s , H , and \mathbf{p} , yielding

$$u_2^{\text{inc}}(\mathbf{r}, t) = -w(t-s; H)a(t-\mathbf{p}\cdot\mathbf{r}). \quad (86)$$

In all cases the reference solution $u_{\text{ref}}(\mathbf{r}, t)$ was equated to the FTH-SS solution $u^I(\mathbf{r}, t)$ (equation (16)) with sufficiently fine discretizations and a sufficiently large frequency interval I . In particular, these computations incorporate the singularity subtraction method, but do not include the asymptotic expansion (80). Convergence of $u^I(\mathbf{r}, t)$ to near machine precision was assessed by refining the boundary integral equation discretization, increasing the size of the frequency interval I , and enlarging the number of integration frequencies used.

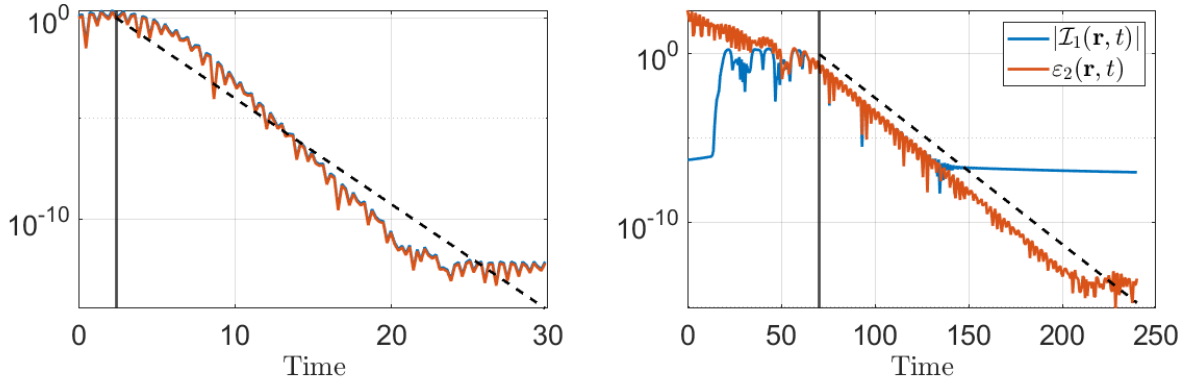


Figure 2: Numerical illustration of the asymptotic behavior of $\mathcal{I}_1(\mathbf{r}, t)$ and $\mathcal{I}_2(\mathbf{r}, t)$. Both panels use the open circle located on the left of Figure 1 with the evaluation point set at $\mathbf{r} = (0, 0)$. The left panel corresponds to Gaussian incidence (84), and includes the reference curve $e^{-1.21(t-1.21/\sigma^2)}$ (dashed line), shown for $t \geq 1.21/\sigma^2$, with the time $t = 1.21/\sigma^2$ indicated by a vertical line. The right panel corresponds to the chirp incident field and for reference additionally displays the function $e^{-0.5(t-70)}$ (dashed line) for $t \geq 70$, with the time $t = 70$ being marked by a black line. In both panels, the vertical black line indicates the onset of exponential decay of $\varepsilon_2(\mathbf{r}, t)$, as predicted by (80) and (81).

This section is organized as follows: Section 6.1 illustrates the convergence of the asymptotic expansion introduced in Section 4.2, along with the fast time-decay of the regularized integral $\mathcal{I}_1(\mathbf{r}, t)$. Section 6.2 then demonstrates the effectiveness of the IE algorithm in capturing all resonances relevant for the computation of the solution u for a given incident field. The regularizing effect of the SS approach (Section (4)) is examined in Section 6.3, followed by an example in Section 6.4 that demonstrates how the singularity-subtraction technique enhances the convergence of the quadrature rules presented in Section 2.3. Sections 6.5 and 6.6, finally, present applications of the full FTH-SS method across a range of illustrative examples.

$$\varepsilon_2(\mathbf{r}, t) = \left| \mathcal{I}_2(\mathbf{r}, t) + \sum_{n=1}^{N_h(I)} i c_{\mathbf{p}, n}(\mathbf{r}) A(\rho_n) e^{-i\rho_n t} \right|. \quad (87)$$

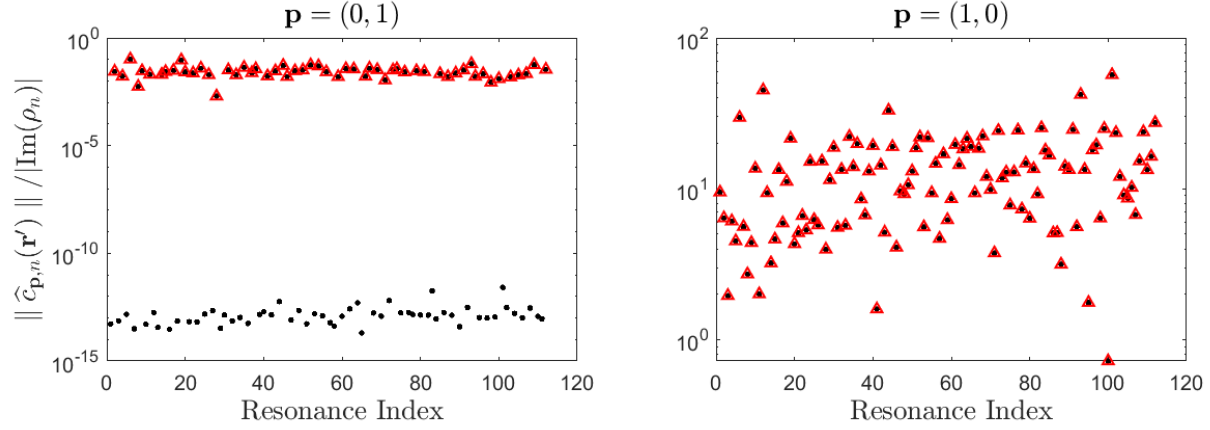


Figure 3: Value of the metric (88) at $\omega = \text{Re}(\rho_n)$ for complex resonances produced by the RE and IE algorithms (shown black dots and red triangles, respectively) for the scattering problem described in the text for incidence directions pointing into the circle opening (left panel) and “tangential” to the circle opening (right panel). As indicated in the text, all the resonances “relevant” for the corresponding time-domain problem are obtained with near machine-precision accuracy.

6.1 Numerical demonstration of the asymptotic character of the quantities \mathcal{I}_1 and \mathcal{I}_2

This section demonstrates, for two different test cases, the asymptotic character of the expansion developed in Section 4.2 for the quantity $\mathcal{I}_2(\mathbf{r}, t)$, as well as the fast decay of the integral $\mathcal{I}_1(\mathbf{r}, t)$, as discussed in Section 4.3. In view of (80) and (81) the error in the aforementioned asymptotic expansion of \mathcal{I}_2 is given by

The first test case assumes an incident field of the form u_1^{inc} in (84) with parameter values $\mathbf{p} = (0, 1)$, $\omega_0 = 8.5$ and $\sigma = \sqrt{0.5}$, together with subtraction of the singularities in the box \mathcal{M}_h^I (55) with $h = 0.5$ and interval $I = [4, 13]$. (The Gaussian function (84) is smaller than machine precision outside the interval I .) Under these conditions, the left panel of Figure 2 displays $|\mathcal{I}_1(\mathbf{r}, t)|$ (blue line) and $\varepsilon_2(\mathbf{r}, t)$ (orange line) at the point $\mathbf{r} = (0, 0)$. We see that $|\mathcal{I}_1(\mathbf{r}, t)|$ decays as rapidly as ε_2 in this case, suggesting that both of these quantities are characterized by singularities located above the line $\text{Im}(\omega) > h$. The dashed-line in the figure, which displays the function $e^{-1.21(t-1.21/\sigma^2)}$, shows that $\varepsilon_2(\mathbf{r}, t)$ decays faster than $O(e^{-h(t-h/\sigma^2)})$. (The value -1.21 was determined by computing all complex resonances in the box \mathcal{M}_2^I (55) by means of the RE algorithm, upon which it was found that all complex resonances with real part in I , and imaginary part in $[-1.21, -0.5]$ have negligible residues (to the order of machine precision)). The solid black line in the figure marks the time $t = 1.21/\sigma^2$ after which, according to (81), the exponential decay of $\varepsilon_2(\mathbf{r}, t)$ is set to start.

For the second test case the chirp incidence u_2^{inc} (86) was used, with parameter values $s = 40$, $H = 30$ and $\mathbf{p} = (0, 1)$ (so that $T^{\text{inc}} = 70$), with subtraction of all singularities in the box \mathcal{M}_h^I (55) with $h = 0.5$, and using $I = [-17, 17]$ —a frequency interval which, clearly, gives rise to significant zero-frequency content in the incidence field. The right panel in Figure 2 again displays $|\mathcal{I}_1(\mathbf{r}, t)|$ (blue line) and $\varepsilon_2(\mathbf{r}, t)$ (orange line) at the point $\mathbf{r} = (0, 0)$. Here the zero frequency content (i.e., the values along Γ of the Fourier transform of u_2^{inc} at $\omega = 0$) is of the order of 10^{-5} . As in the first test case, the figure shows that $|\mathcal{I}_1(\mathbf{r}, t)|$ decays exponentially—but only up to the $O(10^{-5})$ value inherent in the zero frequency content, which would not be observed in a 3D context, and which, as shown in [6], can be accounted for inexpensively in the 2D case as well. The dashed-line in the figure displays the function, $e^{-0.5(t-70)}$, and a vertical line is included at $t = 70$, which marks the time at which, according to (80) the the exponential decay of $\varepsilon_2(\mathbf{r}, t)$ is set to start.

6.2 Adaptive IE algorithm singularity-capturing character

The examples presented in this section demonstrate the ability of the IE method (Algorithm 1), with a given incident field $B_{\mathbf{p}}$, to reliably capture all complex resonances which are relevant to the time domain problem, with incident field $B_{\mathbf{p}}$, up to the level of error inherent in the numerical evaluation of both the time-domain solution and the singularities and residues themselves. As discussed in the introduction to Section 3.3, a useful metric on the relevance of a resonances pair $(\rho_n, \hat{c}_{\mathbf{p},n})$ is given by the L^2 norm

$$\| \hat{c}_{\mathbf{p},n}(\mathbf{r}') \|_{L^2(\Gamma)} / |\omega - \rho_n| \quad (88)$$

of the contribution $\hat{c}_{\mathbf{p},n}(\mathbf{r}')/(\omega - \rho_n)$ of the pair to the integral density and, thus, via (56)–(59), to the scattered field u . Thus, using the open circle displayed on the left most panel of Figure 1 for the examples in this section, Algorithm 1 was applied to obtain the complex resonances in the box \mathcal{M}_h^I (55) with $I = [30, 50]$, and $h = 0.2$. For these demonstrations two different incident directions were used, namely, incidence normal to the opening ($\mathbf{p} = (0, 1)$), and incidence at a 45° angle from the opening ($\mathbf{p} = (1, 0)$). The tolerance $\varepsilon_{\text{tol}} = 10^{-10}$ was used for the AAA portion of the computations, and in each case the integral operator S_ω^N (35) was discretized to an error level matching the tolerance.

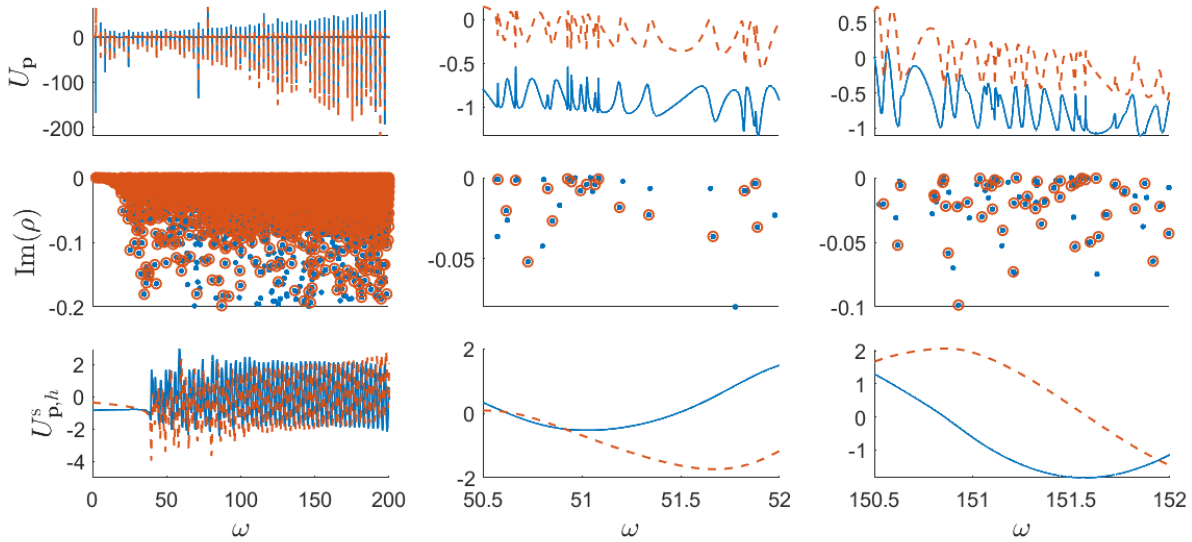


Figure 4: Top and bottom rows: Solutions $U_{\mathbf{p}}(\mathbf{r}, \omega)$ and $U_{\mathbf{p},h}^s(\mathbf{r}, \omega)$, respectively, for three frequency ranges. Solid blue and dashed orange curves display the real and imaginary parts of the solutions. Middle row: Poles generated by the RE and IE algorithms, shown as blue dots and orange circles, respectively. A total 4721 poles with real part in $[0, 200]$ and imaginary part in $[-0.2, 0]$ were obtained and used to compute the regularized solution $U_{\mathbf{p},h}^s$.

Noting that the largest value of the relevance metric (88) for $\omega \in I$ is achieved at $\omega = \text{Re}(\rho_n)$, for each complex resonance $\rho_n \in \mathcal{M}_h^I$ computed by the RE algorithm (which, as discussed in Section 3.2, is expected to produce all the resonance pairs in the box \mathcal{M}_h^I), the quantity $\| \hat{c}_{\mathbf{p},n}(\mathbf{r}') \|_{L^2(\Gamma)} / |\text{Im}(\rho_n)|$ is plotted as a black dot in each panel of Figure 3 with resonances ordered according increasing real part. The first and second panels in Figure 3, which were obtained for the incidence directions $\mathbf{p} = (0, 1)$ and $\mathbf{p} = (1, 0)$, respectively, (i.e., pointing into the circle opening and “tangential” to the circle opening, respectively) also display a red triangle for resonances obtained by the IE. As in the in the figure, Algorithm 1 captures all resonances whose relevance metric is not small. We also note that the complex resonances plotted in are all resonances found by the IE algorithm with $h = 0.2$, demonstrating that no false complex resonances are produced by the AAA algorithm.

6.3 Wide frequency-range singularity subtraction example

In order to study the regularizing effect that results from the singularity subtraction method proposed in Section 4.1, in what follows we consider the problem of scattering by the open circle displayed on the second panel of Figure 1, with boundary conditions given by a plane wave with incident direction $\mathbf{p} = (0, 1)$ (normal to the opening). The left, center and right panels in the top row of images in Figure 4 display the real (solid) and imaginary (dotted) parts of $U_{\mathbf{p}}(\mathbf{r}, \omega)$ (33) at the point $\mathbf{r} = (0, 0)$, for ω in the ranges $[0, 200]$, $[50.5, 52]$, and $[150.5, 152]$ respectively. In all cases a large number of sharp spikes in $U_{\mathbf{p}}(\mathbf{r}, \omega)$ can be seen. The second row displays corresponding poles ρ produced by the RE and IE algorithms as blue dots and orange circles, respectively. (Per Remark 5, to achieve an efficient computation, Algorithm 1 was applied to a set of 20 intervals of length 5 and 50 intervals of length 2 in the ranges $[0, 100]$ and $[100, 200]$ respectively.) Comparison of the first and second rows in Figure 4 reveals a clear correspondence between the relevant complex resonances and the spikes in the solution. The bottom row in Figure 4, finally, displays the singularity-subtracted version $U_{\mathbf{p},h}^s(\mathbf{r}, \omega)$ (66) of $U_{\mathbf{p}}$ —which clearly demonstrates the regularizing effect induced by the singularity subtraction procedure. As illustrated in Section 6.4, use of the regularized field $U_{\mathbf{p},h}^s$ greatly enhances the convergence of the FTH Fourier transform procedure that is required for the evaluation of $u^I(\mathbf{r}, t)$.

6.4 Comparison of FTH and FTH-SS

This section compares the character of the FTH and the FTH-SS methods (Sections 2.1 and 5) in the contexts of trapping and non-trapping obstacles. As expected, the FTH-SS method provides significant advantages for trapping obstacles, and it essentially coincides with the FTH method for non-trapping obstacles. The test cases considered use the Gaussian incident field (84) with incident direction $\mathbf{p} = (1, 1)$ and $\sigma = 0.679$. Two center frequencies are considered, namely $w_0 = 95$ and $w_0 = 195$; with these selections the corresponding Gaussian functions vanish up to machine precision outside the frequency intervals $I = [90, 100]$ and $I = [190, 200]$, respectively. In each case, reference solutions $u_{\text{ref}}(\mathbf{r}, t)$ were obtained as detailed in the introduction to Section 6.

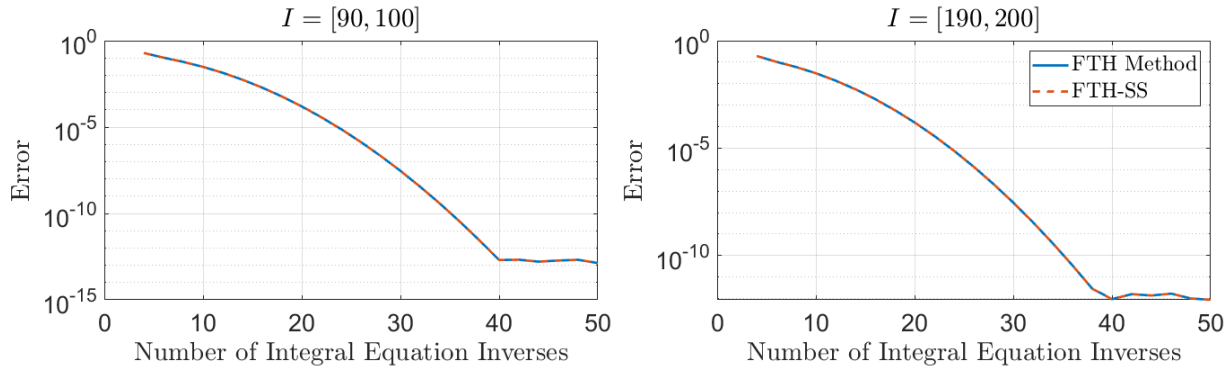


Figure 5: FTH and FTH-SS solution errors for the closed-circle scatterer, as a function of the number of integral equation inverses used. Due to its non-trapping nature, this scatterer does not generate complex resonances near the real axis. Consequently, the FTH-SS method performed no actual singularity subtraction, and its results coincide with those of the standard FTH method in this case.

The first example considers scattering by a closed circular obstacle of radius 1, centered at the origin. This is a non-trapping obstacle and therefore does not produce complex resonances near the real axis. A reference solution $u_{\text{ref}}(\mathbf{r}, t)$ at the point $\mathbf{r} = (0, -1.3)$ and at 500 equispaced times in the interval $[0, 20]$ was used for evaluation of errors. Figure 5 displays the maximum all-time error for both the FTH

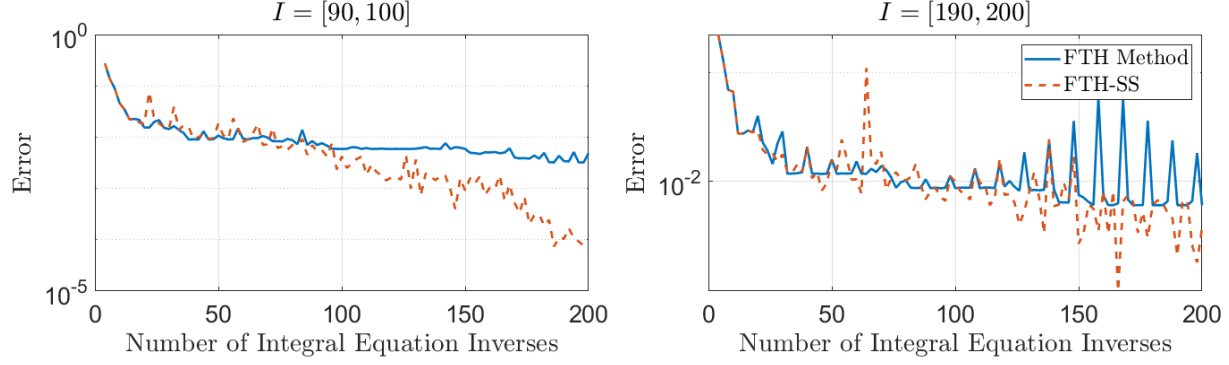


Figure 6: FTH and FTH-SS solution errors for the open circle scatterer depicted on the leftmost panel in Figure 1, as a function of the number of integral equation inverses used. Since a number $J < 200$ of inverses was used for these test cases, the FTH-SS method did not trigger the IE-algorithm’s adaptivity.

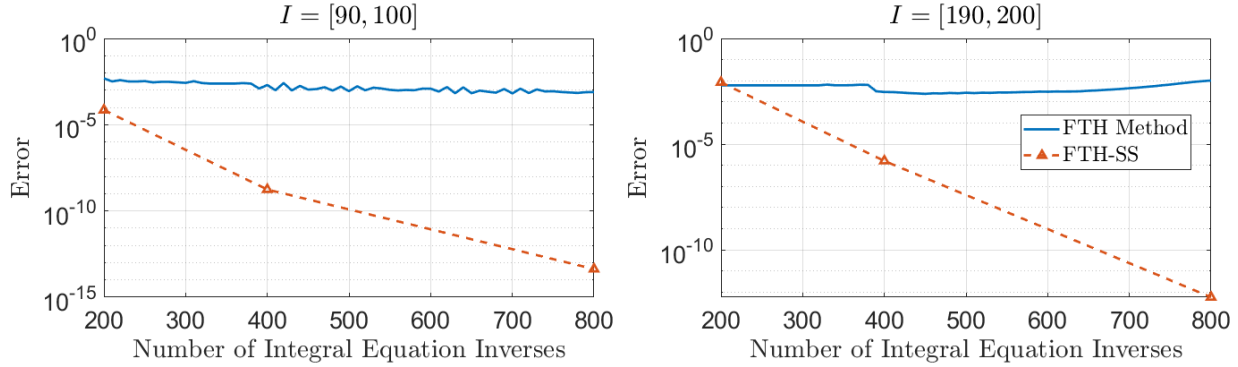


Figure 7: Same as Figure 6 but using a different range of numbers of integral equation inverses—for which the IE-algorithm’s adaptivity was triggered. The triangles mark the errors corresponding to three different numbers of inverses actually used by FTH-SS method—which are determined by each one of the three adaptivity levels triggered in the adaptive IE method.

and FTH-SS methods as functions of the number of integral-equation solves (equivalently, the number of frequencies) used to compute the inverse Fourier transform (15). The left and right panels in the figure correspond to incident fields with non-vanishing frequency content supported in the intervals $I = [90, 100]$ and $I = [190, 200]$, respectively. Following the recommendation in Section 3.3.1, a non-adaptive version of the IE algorithm was used to produce this figure, since the number of frequencies J —which reaches up to $J = 50$ in the figure—satisfies the condition $J < 200$ and therefore does not trigger adaptivity. In particular, the same number of integral equation inverses was used by the FTH and FTH-SS method in this case: as no complex resonances were found by the *IE* algorithm, the FTH and FTH-SS methods actually coincide in this case. As demonstrated by the second example in this section, the situation differs markedly in the case of scattering by a trapping obstacle: in such cases, the FTH-SS method can significantly outperform the FTH method.

The second example in this section concerns scattering by the open circle presented on the leftmost panel in Figure 1, with the same incident fields as in the first example. A reference solution $u_{\text{ref}}(\mathbf{r}, t)$ at the point $\mathbf{r} = (0, 0)$ and at 500 equispaced times in the interval $[0, 120]$ was used for error evaluation. The RE algorithm produced 130 and 192 complex resonances in the box \mathcal{M}_h^I with $h = 0.3$ for the intervals $I = [90, 100]$ and $I = [190, 200]$, respectively. Maximum solution errors—evaluated at $\mathbf{r} = (0, 0)$ over 500 equally spaced time points in the interval $[0, 120]$ —for incident fields with frequency content in the intervals

$I = [90, 100]$ and $I = [190, 200]$ are shown on the left and right panels, respectively, in both Figures 6 and 7.

As in the first example of this section, the results in Figure 6 were obtained using the IE algorithm without adaptivity, since only frequency numbers $J < 200$ were used in this case. In particular, this figure demonstrates that even without the adaptive version of the IE algorithm, the FTH-SS method offers a significant advantage. As shown in Figure 7, an even greater improvement is achieved when frequency numbers $J \geq 200$ are used in combination with the fully adaptive IE algorithm. In Figure 7 only three numbers-of-inverses, 200, 400 and 800, marked as triangular error points, were used for the FTH-SS method. These values correspond to splitting the interval I into 1, 2 and 4 subintervals respectively, as part of the adaptive IE algorithm with initial input $J = 200$ in the interval I . As additional reference points we report that for the intervals $I = [90, 100]$ and $I = [190, 200]$ and utilizing as many as 10,000 inverses, the FTH method (without singularity subtraction) produced solutions with errors of $1.2 \cdot 10^{-8}$ and $5.0 \cdot 10^{-5}$, respectively.

6.5 Time-domain resonance build up

The FTH-SS algorithm's ability to deliver accurate solutions over long time intervals makes it well-suited for studying the buildup of resonances in highly trapping cavities. To demonstrate this capability, we consider two examples: a circle with an opening and a rocket-shaped scatterer with an opening.

For our first example we utilize the large opening-circle scatterer presented in the leftmost panel in Figure 1, and we use the Gaussian incident field (84) with $\omega_0 = 50$, $\sigma^2 = 0.5$, $\mathbf{p} = (0, 1)$, $I = [45.5, 54.5]$, and subtracting resonances produced by the adaptive IE algorithm in the box \mathcal{M}_h^I with $h = -0.5$. Various snapshots of the absolute value of the real part of the total field are plotted in Figure 8, which highlight several resonant structures which change with time as well as the slow decay of the scattered field after the incident field vanishes on the scattering boundary.

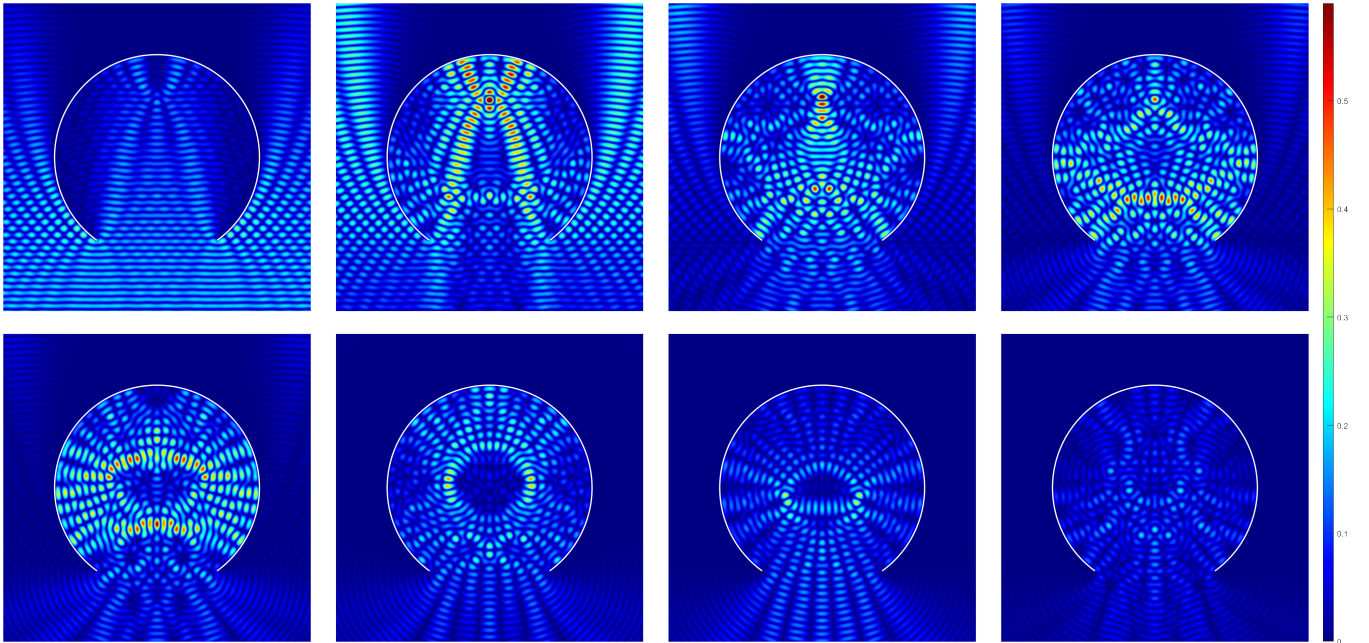


Figure 8: Temporal evolution of scattering from the open circle, shown at an increasing sequence of times from left to right and top to bottom. Each panel shows the absolute value of the real part of the total field. Distinct resonant structures are visible both during and after excitation by the incident field.

The second example in this section demonstrates the time domain excitation of a localized resonance in the rocket-shaped scatterer depicted in the third panel in Figure 1, using the Gaussian incident field (84)

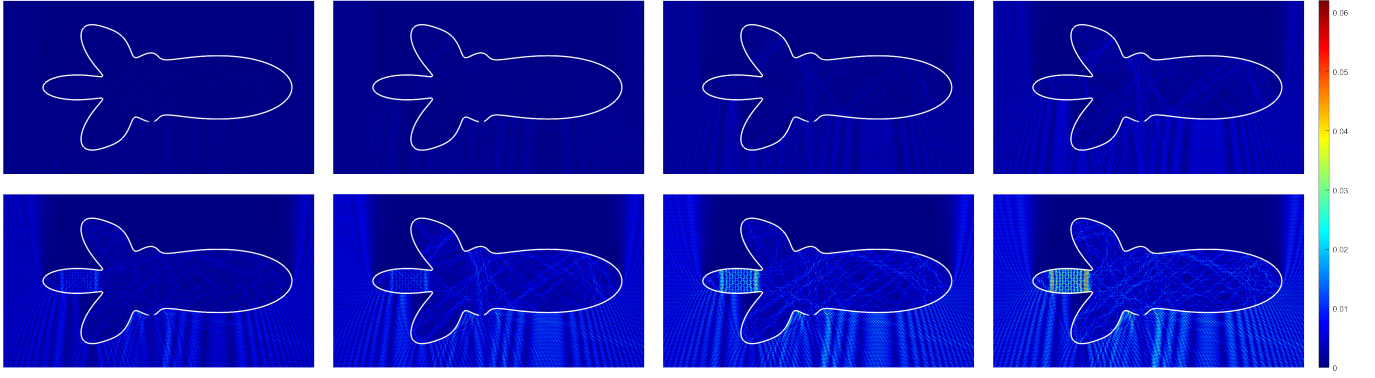


Figure 9: Same as in Figure 8 but for the rocket-shaped structure depicted in Figure 1. A pronounced localized resonance becomes clearly visible as it develops in the left finger of the rocket structure.

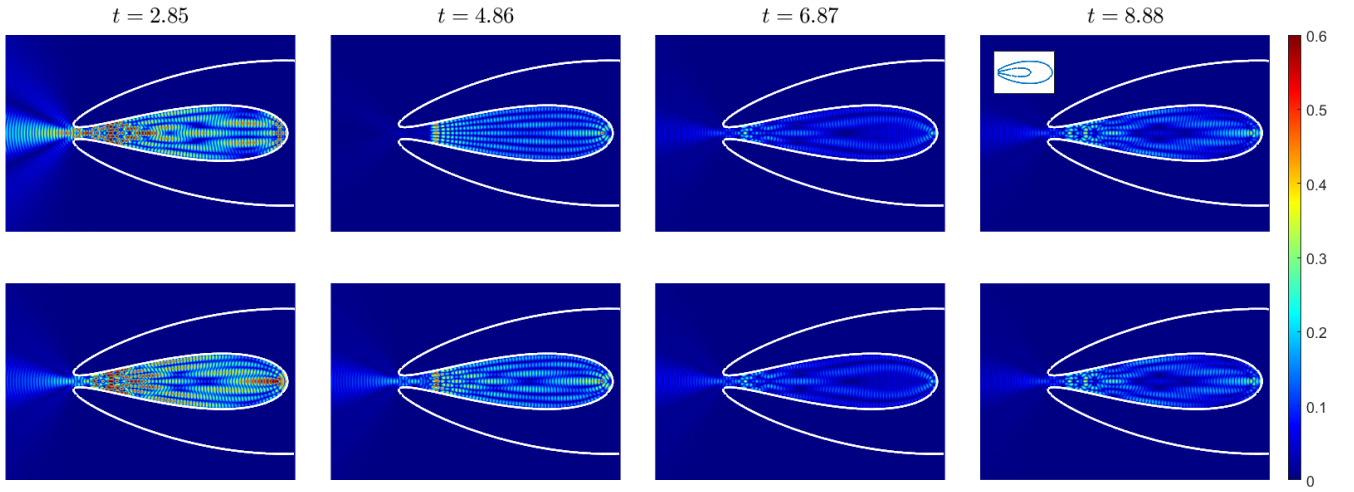


Figure 10: Top row: Temporal evolution of fields scattered from a highly trapping closed curve at an increasing sequence of times. Bottom row. Corresponding values of the singularity expansion (80). For reference the closed scatterer is displayed on the top-right panel.

with $\omega_0 \approx 399.969$, (a selection that corresponds to the eigenfunction displayed in [15, Fig. 8]), $\sigma^2 = 0.0011$, and $I = [399.7695, 400.1695]$. Figure 9 displays the the absolute value of the real part of the total field for various times. A strong localized resonance is seen to build up in the rocket's left finger.

6.6 Validity of the singularity expansion in the asymptotic regime

This section presents a variety of numerical results illustrating the theoretical discussion in Section 4.3, with a focus on the convergence of the singularity expansion (82) to the time-domain solution at sufficiently large times. To this end we examine two scattering structures: the trapping closed scatterer presented in the rightmost panel in Figure 1 and Figures 10, and a whispering-gallery configuration depicted in Figures 11 and 12.

In the first case, using the incident field defined in equation (84), with parameters $\mathbf{p} = (1, 0)$, $\sigma^2 = 2.714$, $\omega_0 = 300$, $I = [290, 310]$, and a singularity-box depth of $h = 0.3$, the corresponding scattered fields were computed—whose absolute values are displayed at various times in the top row of Figure 10. The associated asymptotic singularity-expansion approximations are presented in the bottom row. The snapshot at $t = 2.85$

corresponds to a time point shortly after the incident field has passed the scatterer. Comparison of the top and bottom rows clearly demonstrates the rapid convergence of the singularity expansion to the true solution at later times, while also indicating that the singularity expansion alone does not accurately capture the early-time behavior.

The whispering-gallery example, in turn, is considered in Figures 11 and 12. This scattering structure, which consists of two parabolic open curves, is illuminated by a chirp incident field (85) with parameters $\mathbf{p} = (1, -1)$, $s = 17.5$, $H = 7.5$, $I = [-20, 20]$, and a singularity-box depth of $h = 0.3$. For this choice of parameters the incident field is supported in the time interval $10 \leq t \leq 25$. The top row of Figure 11, which displays the absolute value of the total field at various times, while the bottom row presents the corresponding values of asymptotic singularity expansion (82) at the corresponding times. Comparison of these two rows of images shows that, in agreement with the analysis in Section 4.2, the singularity expansion suffers from significant errors before the $t = 25$ incident-field extinction time, and that the errors decrease rapidly at later times. Figure 12 demonstrates the ability of the singularity expansion to correctly capture the late multiple scattering whispering gallery events.

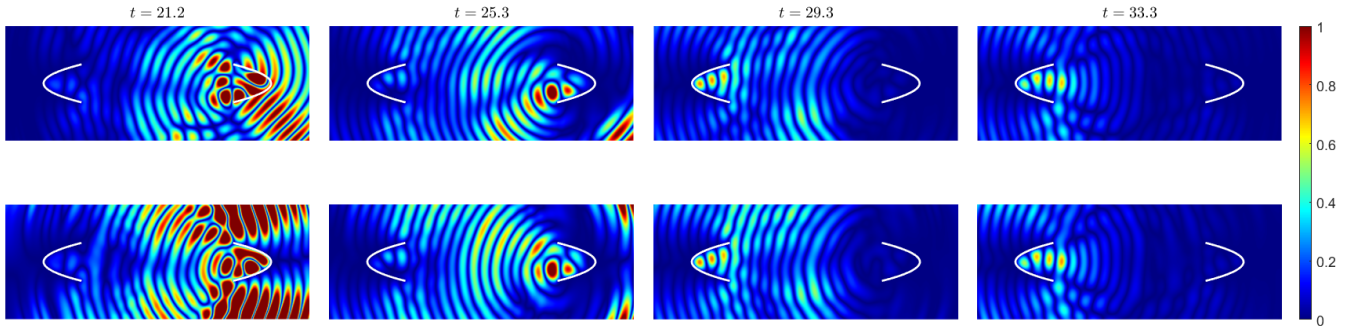


Figure 11: Same as Figure 10 but for a whispering-gallery scattering structure. In agreement with the analysis in Section 4.2, the singularity expansion suffers from significant errors before the $t = 25$ incident-field extinction time, and the error decrease rapidly at later times.

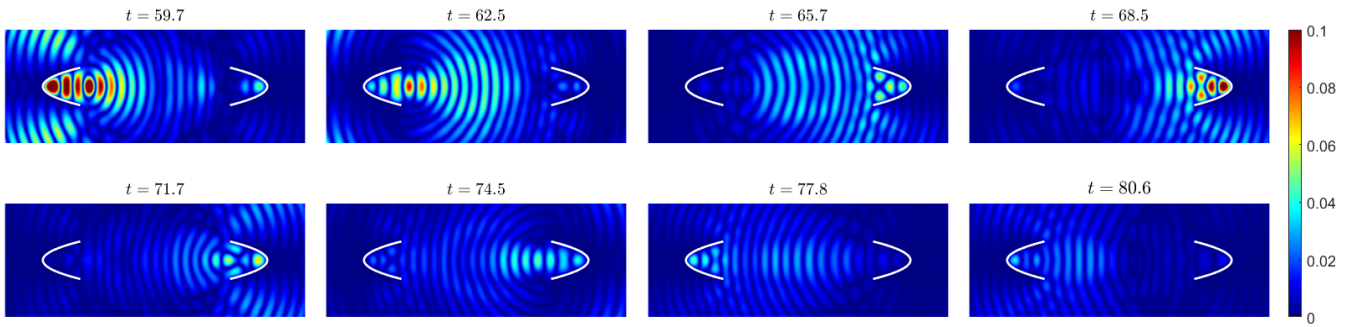


Figure 12: Late-time multiple-scattering events in the whispering-gallery structure. The absolute value of the singularity expansion approximation is displayed at several time points, demonstrating the expansion's ability to capture complex late-time scattering behavior. (Note: The color scale used here differs from the one employed in Figure 11.)

7 Conclusions

This paper presented a singularity subtraction technique that, building on Fourier-transform-based methods [5], enables efficient computation of time-domain scattering from trapping obstacles. Central to the approach is a novel Incidence Excited (IE) algorithm, which, relying only on real-frequency scattering solutions, facilitates the efficient evaluation of all complex resonances and residues *relevant* to the subtraction method. The method is completed by evaluation of the fields associated with the subtracted singularities via a combination of a simple and inexpensive numerical technique together with a large-time asymptotic expansion. In fact, on the basis of a wide range of numerical examples presented in this paper, a related and well-known “singularity expansion” was shown to generally accurately capture the late-time behavior of the scattered fields—even for strongly trapping structures where theoretical justification is not yet established. Importantly, the proposed numerical method is rigorously valid irrespective of asymptotic validity of the singularity expansion. A range of numerical examples demonstrated the method’s high efficiency and accuracy.

8 Acknowledgments

The authors gratefully acknowledge support from the Air Force Office of Scientific Research and the National Science Foundation under contracts FA9550-21-1-0373, FA9550-25-1-0015, DMS-2109831, and NSF Graduate Research Fellowship No. 2139433.

A Appendix: Complex resonances via the combined field formulation

As is well known [53], the analytic continuation of the Dirichlet-Helmholtz solution operator \mathcal{U}_ω^c to the domain $\text{Im } \omega < 0$ can be constructed using the inverse of the operator $C_{\omega,0}$ (i.e., the inverse of $C_{\omega,\eta}$ with $\eta = 0$). Unfortunately, however, the operator $(C_{\omega,0})^{-1}$ has certain poles on the real axis that do not correspond to poles of the solution operator \mathcal{U}_ω^c . These real poles can be avoided by utilizing the operator $(C_{\omega,\eta})^{-1}$ with $\eta \neq 0$, instead. But, like $(C_{\omega,0})^{-1}$, the operator $(C_{\omega,\eta})^{-1}$ has complex poles that do not correspond to the poles of \mathcal{U}_ω^c . Fortunately, as shown in Theorem 1 below, for any η whose sign differs from that of ω , the poles of the inverse operator $(C_{\omega,\eta})^{-1}$ in the lower half-plane $\text{Im } \omega \leq 0$ coincide with the poles of \mathcal{U}_ω^c .

Lemma 1. *Let ω and η satisfy $\text{Im}(\omega) < 0$, $\text{Re}(\omega) > 0$ (resp. $\text{Re}(\omega) < 0$), and $\eta < 0$ (resp. $\eta > 0$). Then $\mathcal{C}_\eta : H^{1/2}(\Gamma) \rightarrow H_{loc}^1(\Omega^e)$ is an injective operator.*

Proof. The proof relies on the fact that, for a given $\psi \in H^{1/2}(\Gamma)$ and defining the function $U(\mathbf{r}, \omega) = \mathcal{C}_\eta[\psi](\mathbf{r}, \omega)$ for $\mathbf{r} \notin \Gamma$, then if U vanishes identically in Ω^e then U and ψ satisfy the relation

$$-\frac{2}{c} \text{Re}(\omega) \text{Im}(\omega) \int_{\Omega^i} |U|^2 dx = \eta \int_{\partial\Omega} |\psi|^2 ds, \quad (89)$$

where $\Omega^i := \mathbb{R}^2 \setminus \Omega \cup \Gamma$. This can be established as in [17, Theorem 3.33] by noting that the necessary jump relations are valid [40, Theorem 6.11] in the functional setting considered here. In the case $\text{Re}(\omega) > 0$ the left-hand term in (89) is non-negative, which, since $\eta < 0$, implies that ψ vanishes identically, and the injectivity of \mathcal{C}_η follows in this case. The case $\text{Re}(\omega) < 0$, $\eta > 0$ follows similarly. \square

Theorem 1. *Let $\omega \in \mathbb{C}$ such that $\text{Re}(\omega) > 0$ (resp. $\text{Re}(\omega) < 0$), and let $\eta < 0$ (resp. $\eta > 0$). Then, for $\text{Im}(\omega) \leq 0$, the set of poles of $(C_{\omega,\eta})^{-1}$ coincides with the set of poles of \mathcal{U}_ω^c .*

Proof. Since the double- and single-layer operators (19) are compact, the operator $(C_{\omega,\eta})^{-1}$ is a meromorphic function of ω in the entire complex plane [53, Proposition 7.4], except for a logarithmic branch cut joining $\omega = 0$ and $\omega = \infty$. In view of the representation (47) of the solution operator \mathcal{U}_ω^c it follows that the set of poles of $\mathcal{U}_c(\omega)$ is contained within the set of poles of $(C_{\omega,\eta})^{-1}$.

To show that the converse is also true assume $(C_{\omega,\eta})^{-1}$ has a pole of order m at $\omega = \omega_0$ with $\text{Im}(\omega_0) < 0$. Then there exists an element $B \in H^{1/2}(\Gamma)$ such that

$$(C_{\omega,\eta})^{-1}[B] = (\omega - \omega_0)^{-m} (B_m + B_{m+1}(\omega - \omega_0) + \dots)$$

for a certain sequence $B_j \in H^{1/2}(\Gamma)$, $j \geq m$, with $B_m \neq 0$. Letting $u_m = \mathcal{C}_\eta[B_m]$ it follows that

$$\mathcal{U}_\omega^c[B] = (\omega - \omega_0)^{-m} u_m + O((\omega - \omega_0)^{-m+1}) \quad \text{as } \omega \rightarrow \omega_0.$$

By Lemma 1 $u_m \neq 0$, and, therefore ω_0 is a pole of \mathcal{U}_ω^c . The proof is now complete \square

References

- [1] Jeffrey H. Albert. Genericity of simple eigenvalues for elliptic PDE's. *Proceedings of the American Mathematical Society*, 48(2):413–418, 1975.
- [2] Carlos J.S. Alves and Pedro R.S. Antunes. Wave scattering problems in exterior domains with the method of fundamental solutions. *Numerische Mathematik*, 156:1–20, 2024.
- [3] Faisal Amlani and Oscar P. Bruno. An FC-based spectral solver for elastodynamic problems in general three-dimensional domains. *Journal of Computational Physics*, 307:333–354, 2016.
- [4] Thomas G. Anderson and Oscar P. Bruno. "Bootstrap domain of dependence": Bounds and time decay of solutions of the wave equation, 2022.
- [5] Thomas G. Anderson, Oscar P. Bruno, and Mark Lyon. High-order, dispersionless "fast-hybrid" wave equation solver. Part I: $O(1)$ sampling cost via incident-field windowing and recentering. *SIAM Journal on Scientific Computing*, 42(2):A1348–A1379, 2020.
- [6] Thomas G. Anderson, Oscar P. Bruno, and Mark Lyon. "Fast-hybrid" wave equation solver part II: 3D window tracking, 2D asymptotics tracking, general incident fields and remote field evaluation. In preperation.
- [7] Junko Asakura, Tetsuya Sakurai, Hiroto Tadano, Tsutomu Ikegami, and Kinji Kimura. A numerical method for nonlinear eigenvalue problems using contour integrals. *JSIAM Letters*, 1:52–55, 2009.
- [8] Lehel Banjai. Multistep and multistage convolution quadrature for the wave equation: algorithms and experiments. *SIAM Journal on Scientific Computing*, 32(5):2964–2994, 2010.
- [9] C. E. Baum. The singularity expansion method. In Leopold B. Felsen, editor, *"Transient Electromagnetic Fields"*, pages 129–179. Springer Berlin Heidelberg, Berlin, Heidelberg, 1976.
- [10] Timo Betcke, Simon N. Chandler-Wilde, Ivan G. Graham, Stephen Langdon, and Marko Lindner. Condition number estimates for combined potential integral operators in acoustics and their boundary element discretisation. *Numerical Methods for Partial Differential Equations*, 27(1):31–69, 2011.
- [11] Timo Betcke, Nicolas Salles, and Wojciech Smigaj. Overresolving in the laplace domain for convolution quadrature methods. *SIAM Journal on Scientific Computing*, 39(1):A188–A213, 2017.

- [12] Wolf-Jürgen Beyn. An integral method for solving nonlinear eigenvalue problems. *Linear Algebra and its Applications*, 436(10):3839–3863, 2012.
- [13] Oscar P. Bruno and Stéphane K. Lintner. A high-order integral solver for scalar problems of diffraction by screens and apertures in three-dimensional space. *Journal of Computational Physics*, 252:250–274, 2013.
- [14] Oscar P. Bruno and Mark Lyon. High-order unconditionally stable FC-AD solvers for general smooth domains i. basic elements. *Journal of Computational Physics*, 229(6):2009–2033, 2010.
- [15] Oscar P. Bruno, Manuel A. Santana, and Lloyd N. Trefethen. Evaluation of resonances: adaptivity and AAA rational approximation of randomly scalarized boundary integral resolvents. *arXiv preprint arXiv:2405.19582*, 2024.
- [16] Oscar P. Bruno and Tao Yin. Multiple-scattering frequency-time hybrid solver for the wave equation in interior domains. *Mathematics of Computation*, 93(346):551–587, 2024.
- [17] David L. Colton and Rainer Kress. *Integral Equation Methods in Scattering Theory*. John Wiley & Sons Inc., New York, 1983.
- [18] David L. Colton and Rainer Kress. *Inverse acoustic and electromagnetic scattering theory, 4th Edition*. Springer, 2019.
- [19] Marion Darbas, Eric Darrigrand, and Yvon Lafranche. Combining analytic preconditioner and fast multipole method for the 3-d helmholtz equation. *Journal of Computational Physics*, 236:289–316, 2013.
- [20] C. Dolph and Soon Cho. On the relationship between the singularity expansion method and the mathematical theory of scattering. *IEEE Transactions on Antennas and Propagation*, 28(6):888–897, 1980.
- [21] Victor Domínguez, Ivan G. Graham, and Tatiana Kim. Filon–Clenshaw–Curtis rules for highly oscillatory integrals with algebraic singularities and stationary points. *SIAM Journal on Numerical Analysis*, 51(3):1542–1566, 2013.
- [22] Víctor Domínguez and Catalin Turc. Nyström discretizations of boundary integral equations for the solution of 2d elastic scattering problems. *Journal of Computational and Applied Mathematics*, 440:115622, 2024.
- [23] Tobin A. Driscoll, Nicholas Hale, and Lloyd N. Trefethen. *Chebfun Guide*, 2014. www.chebfun.org.
- [24] Mohamed El-Guide, Agnieszka Międlar, and Yousef Saad. A rational approximation method for solving acoustic nonlinear eigenvalue problems. *Engineering Analysis with Boundary Elements*, 111:44–54, 2020.
- [25] Stefan Güttel, Daniel Kressner, and Bart Vandereycken. Randomized sketching of nonlinear eigenvalue problems. *SIAM Journal on Scientific Computing*, 46(5):A3022–A3043, 2024.
- [26] Stefan Güttel and Françoise Tisseur. The nonlinear eigenvalue problem. *Acta Numerica*, 26:1–94, 2017.
- [27] Christophe Hazard and François Loret. The singularity expansion method applied to the transient motions of a floating elastic plate. *ESAIM: Mathematical Modelling and Numerical Analysis*, 41(5):925–943, 2007.

- [28] E. Heyman and L. Felsen. A wavefront interpretation of the singularity expansion method. *IEEE Transactions on Antennas and Propagation*, 33(7):706–718, 1985.
- [29] Mitsuru Ikawa. Decay of solutions of the wave equation in the exterior of two convex obstacles. *Osaka Journal of Mathematics*, 19(3):459–509, 1982.
- [30] Frédéric Klopp and Maciej Zworski. Generic simplicity of resonances. *Helvetica Physica Acta*, 68(6):531–538, 1995.
- [31] David Lafontaine, Euan A. Spence, and Jared Wunsch. For most frequencies, strong trapping has a weak effect in frequency-domain scattering. *Communications on Pure and Applied Mathematics*, 74(10):2025–2063, 2021.
- [32] Peter D. Lax, Cathleen S. Morawetz, and Ralph S. Phillips. Exponential decay of solutions of the wave equation in the exterior of a star-shaped obstacle. In *Selected Papers Volume II*, pages 5–14. Springer, 2005.
- [33] Peter D. Lax and Ralph Saul Phillips. Decaying modes for the wave equation in the exterior of an obstacle. *Communications on Pure and Applied Mathematics*, 22(6):737–787, 1969.
- [34] Pieter Lietaert, Karl Meerbergen, Javier Pérez, and Bart Vandereycken. Automatic rational approximation and linearization of nonlinear eigenvalue problems. *IMA Journal of Numerical Analysis*, 42(2):1087–1115, 2022.
- [35] Stéphane K. Lintner and Oscar P. Bruno. A generalized Calderón formula for open-arc diffraction problems: theoretical considerations. *Proceedings of the Royal Society of Edinburgh*, 145(2):331–364, 2015.
- [36] C. Lubich. On the multistep time discretization of linear initial-boundary value problems and their boundary integral equations. *Numerische Mathematik*, 67(3):365–389, 1994.
- [37] R.C. MacCamy. Low frequency acoustic oscillations. *Quarterly of Applied Mathematics*, 23(3):247–255, 1965.
- [38] R.B. Marks. The singular function expansion in time-dependent scattering. *IEEE transactions on antennas and propagation*, 37(12):1559–1565, 1989.
- [39] Paul A Martin. *Time-domain scattering*, volume 180. Cambridge University Press, 2021.
- [40] William Charles Hector McLean. *Strongly elliptic systems and boundary integral equations*. Cambridge University Press, 2000.
- [41] Michael H. Meylan and Colm J. Fitzgerald. The singularity expansion method and near-trapping of linear water waves. *Journal of fluid mechanics*, 755:230–250, 2014.
- [42] Michael H. Meylan and Marko Tomic. Complex resonances and the approximation of wave forcing for floating elastic bodies. *Applied ocean research*, 36:51–59, 2012.
- [43] Ryota Misawa, Kazuki Niino, and Naoshi Nishimura. Boundary integral equations for calculating complex eigenvalues of transmission problems. *SIAM Journal on Applied Mathematics*, 77(2):770–788, 2017.
- [44] Cathleen S. Morawetz. The decay of solutions of the exterior initial-boundary value problem for the wave equation. *Communications on Pure and Applied Mathematics*, 14(3):561–568, 1961.

- [45] Cathleen S. Morawetz. Exponential decay of solutions of the wave equation. *Communications on Pure and Applied Mathematics*, 19(4):439–444, 1966.
- [46] LA Muraveĭ. On the asymptotic behavior, for large values of the time, of solutions of exterior boundary value problems for the wave equation with two space variables. *Mathematics of the USSR-Sbornik*, 35(3):377, 1979.
- [47] Yuji Nakatsukasa, Olivier Sète, and Lloyd N. Trefethen. The AAA algorithm for rational approximation. *SIAM Journal on Scientific Computing*, 40(3):A1494–A1522, 2018.
- [48] Davide Pradovera, Ralf Hiptmair, and Ilaria Perugia. Surrogate modeling of resonant behavior in scattering problems through adaptive rational approximation and sketching. *arXiv preprint arXiv:2503.10194*, 2025.
- [49] Alexander G. Ramm. Mathematical foundations of the singularity and eigenmode expansion methods (sem and eem). *Journal of Mathematical Analysis and Applications*, 86(2):562–591, 1982.
- [50] Ian H. Sloan and William E. Smith. Product integration with the clenshaw-curtis points: implementation and error estimates. *Numerische Mathematik*, 34(4):387–401, 1980.
- [51] Olaf Steinbach and Gerhard Unger. Combined boundary integral equations for acoustic scattering-resonance problems. *Mathematical Methods in the Applied Sciences*, 40(5):1516–1530, 2017.
- [52] Siu-Hung Tang and Maciej Zworski. Resonance expansions of scattered waves. *Communications on Pure and Applied Mathematics: A Journal Issued by the Courant Institute of Mathematical Sciences*, 53(10):1305–1334, 2000.
- [53] Michael E. Taylor. *Partial differential equations. II*. Springer-Verlag, New York, 1996.
- [54] Boris Vainberg. *Asymptotic methods in equations of mathematical physics*. CRC Press, 1989.
- [55] Jörg Waldvogel. Fast construction of the Fejér and Clenshaw–Curtis quadrature rules. *BIT Numerical Mathematics*, 46:195–202, 2006.
- [56] P Werner. Low frequency asymptotics for the reduced wave equation in two-dimensional exterior spaces. *Mathematical methods in the applied sciences*, 8(1):134–156, 1986.
- [57] B. Wilks, M.H. Meylan, F. Montiel, and S. Wakes. Generalized eigenfunction expansion and singularity expansion methods for two-dimensional acoustic time-domain wave scattering problems. *Proceedings of the Royal Society A*, 480(2297):20230845, 2024.